

Anatomy of galactic star formation history: Roles of different modes of gas accretion, feedback, and recycling

Masafumi Noguchi¹★

¹*Astronomical Institute, Tohoku University, 6-3, Aramaki, Aoba-ku, Sendai, Miyagi, 980-8578, Japan*

Accepted XXX. Received YYY; in original form ZZZ

ABSTRACT

We investigate how the diverse star formation histories observed across galaxy masses emerged using models that evolve under gas accretion from host halos. They also include ejection of interstellar matter by supernova feedback, recycling of ejected matter and preventive feedback that partially hinders gas accretion. We consider three schemes of gas accretion: the fiducial scheme which includes the accretion of cold gas in low-mass halos and high-redshift massive halos as hinted by cosmological simulations; the flat scheme in which high-mass cold accretion is removed; and finally the shock-heating scheme which assumes radiative cooling of the shock-heated halo gas. The fiducial scheme reproduces dramatic diminishment in star formation rate (SFR) after its peak as observed for the present halo mass $M_{\text{vir}} > 10^{12.5} M_{\odot}$ while other two schemes show reduced or negligible quenching. This scheme reproduces the high-mass slope in the SFR vs. stellar mass relation decreasing toward recent epochs whereas other two schemes show opposite trend which contradicts observation. Success in the fiducial scheme originates in the existence of high-mass cold-mode accretion which retards transition to the slow hot-mode accretion thereby inducing a larger drop in SFR. Aided by gas recycling, which creates monotonically increasing SFR in low-mass halos, this scheme can reproduce the downsizing galaxy formation. Several issues remain, suggesting non-negligible roles of missing physics. Feedback from active galactic nuclei could mitigate upturn of SFR in low-redshift massive halos whereas galaxy mergers could remedy early inefficient star formation.

Key words: galaxies: formation – galaxies: evolution – galaxies: star formation – galaxies: stellar content

1 INTRODUCTION

Recent large scale surveys both from the ground and the space (e.g., SDSS, GALEX, PRIMUS, CANDELS, ZFOURGES) have revealed the properties of galactic star formation across a wide mass range from the local Universe to high redshift utilizing multiwavelength observations (e.g. Martin et al. 2005; Coil et al. 2011; Grogin et al. 2011; Koekemoer et al. 2011; Skelton et al. 2014; Straatman et al. 2016). The most important information derived from these surveys includes the star formation history (SFH) for various masses and the correlation between star formation activity measured by the star formation rate (SFR) and other properties of host galaxies.

Many theoretical attempts have been made to reproduce and interpret the data obtained by the large surveys thereby understanding the galaxy formation process over the cosmic time. They aim to explain not only the observational data directly related to the star formation activity but also other global properties of galaxies such as luminosity and mass functions, colour distributions, sizes, metallicity, gas contents, scaling relations (e.g., Tully-Fisher

relation). They are broadly classified into two categories, namely, cosmological simulations and semi-analytic models.

Cosmological simulations (e.g., Illustris, EAGLE, FIRE, NIHAO, VELA) follow the evolution of dark matter halos and galaxies in the Universe starting from the initial condition prescribed by the assumed cosmology. Growth of dark matter halos and several baryonic processes (e.g., gas heating and cooling on global scales) are directly treated. Due to the limited spatial and time resolution attainable, other local processes such as star formation, stellar evolution, feedback, black hole growth are usually treated as ‘subgrid’ physics. Within this limitation, cosmological simulations are expected to provide the most realistic and direct treatment for galaxy formation. However, the results depend strongly on the prescription for the subgrid physics and much effort has been paid to understand the nature of such a dependence and improve the modelling (e.g. Ceverino & Klypin 2009; Hopkins, Quataert & Murray 2012; Genel et al. 2014; Hopkins et al. 2014; Vogelsberger et al. 2014; Schaye et al. 2015; Wang et al. 2015). Although these simulations provide a powerful tool in making realistic galaxies, their expensive nature sometimes makes it difficult to elucidate the effect of included processes by running a large suit of models.

★ E-mail: noguchi@astr.tohoku.ac.jp (MN)

Semi-analytic models (e.g., GALFORM, L-GALAXIES, GALICS 2.1) play a complementary role to the cosmological simulations. They build on the hierarchical merger history of the dark matter halos taken from the analytical or numerical studies and include various physical processes that govern the evolution of baryonic components (e.g. White & Frenk 1991; Kauffmann, White & Guiderdoni 1993; Lacey et al. 1993; Cole et al. 1994; Somerville & Primack 1999; Croton et al. 2006; Monaco, Fontanot & Taffoni 2007; de Lucia & Blaizot 2007; de Lucia et al. 2010; Guo et al. 2011; Lagos et al. 2014; Lu et al. 2014; Lacey et al. 2016; Croton et al. 2016; Mitchell et al. 2018; Cattaneo et al. 2020). These processes are usually included in parametrized forms and effects of these parameters are investigated. This approach has an advantage that it can explore wide ranges in parameters which is usually difficult for expensive cosmological simulations. The drawback is that the assumptions about baryonic processes affect result more strongly than in cosmological simulations and cannot handle spatial configurations such as galaxy morphology directly.

Currently, these two approaches, sometimes in cooperation, are attaining remarkable success in reproducing a variety of observed characteristics for wide ranges in galaxy masses and cosmological epochs. However, these two methods have a drawback in common that the complicated interplay of employed physical processes poses obstacles to clear interpretation of the obtained results in some cases although this difficulty is partially overcome by running models including different sets of physical processes.

Several studies (e.g., UNIVERSE MACHINE, EMERGE) utilize the abundance matching method and other similar techniques to connect the merger history of dark matter halos predicted by numerical simulations and the observational data for galactic star formation (e.g. Behroozi, Wechsler & Conroy 2013; Behroozi et al. 2019; Moster, Naab & White 2013, 2018; Moster et al. 2021). In short, those studies parametrize the baryonic processes such as the gas accretion rate, the star formation rate, and the gas ejection rate as a function of halo mass and redshift and the parameters are tuned so as to reproduce the observational data. Due to their made-to-measure nature, these approaches are regarded as giving observational constraints rather than theoretical prediction. Nevertheless, they enable linking galaxies at different epochs into continuous evolutionary paths empirically and serve as a valuable testbed for theoretical models. The results from these studies are intensively used in our study for comparison.

We take here a new approach using a simple evolution model of galaxy evolution that includes a minimum set of potentially important processes. By intercomparing models incorporating different gas accretion schemes and different sets of feedback and gas recycling, we aim to isolate the effect of each ingredient. Our modelling is thus in a similar spirit to the 'equilibrium' model of galaxy evolution (e.g. Davé, Finlator & Oppenheimer 2012; Mitra, Davé & Finlator 2015) but does not assume the instantaneous equilibrium of the galactic system. It traces the time evolution of galaxies explicitly without the constraint of equilibrium and is expected to give more realistic treatment. For example, the evolution of gaseous contents in galaxies, set automatically constant with time in the equilibrium model, can be directly traced and compared with the observational data. Mass loading factor for stellar (supernova) feedback is also obtained automatically. Early phase of galaxy evolution driven by efficient gas fuelling likely deviates from the equilibrium condition (Davé, Finlator & Oppenheimer 2012). This phase is an important target of this study so that we think the freedom from equilibrium assumption is a rewarding feature of the present model. Because our model nevertheless involves a number of simplifications, we hope

to reproduce qualitative features of galactic star formation gained by the observation in the first place. We will see, however, that the present model gives quantitatively reasonable description of the observation in some cases. Many previous studies put forward propositions for the respective roles of the physical processes involved in the evolution of stellar contents of galaxies. By constructing the model that satisfies a wide range of observational constraints simultaneously, we try to check these propositions and get a new insight into key physics that governs galactic star formation history.

Our paper is organized as follows. In section 2, we introduce the models we use for tracing galaxy evolution. Section 3 describes and discusses the gas accretion schemes explored in this study. Star formation histories in these schemes are examined in detail and compared with observations in section 4. Section 5 is devoted to the investigation of roles played by the physical processes included in the model. Section 6 presents discussion on several issues for which further study is desired and section 7 summarizes our conclusions.

2 MODELS

We model a disc galaxy as a composite system comprising the halo gas, the interstellar gas, and the stellar disc embedded in a dark matter halo. The baryonic components (the halo gas, the interstellar gas, and the stellar disc) are specified by their masses, the time evolution of which is calculated over the cosmic time. This model is thus 'one-zone' treatment in the sense that the spatial structure of each baryonic component (and the dark matter halo) is not considered except when we calculate the rates of several physical processes as explained later. The physical processes included in our model are the growth of the dark matter halo, the accretion of the halo gas on to the disc (i.e., creation of the interstellar gas), the star formation from the interstellar gas, the ejection of the interstellar gas by supernova feedback, the reincorporation (recycling) of the ejected gas to the interstellar gas, and the prevention of the gas accretion on to the disc. We describe the physical aspect of those processes here and defer numerical details of their implementation to Appendix. We assume the Λ CDM cosmology with parameters $\Omega_M=0.27$, $\Omega_\Lambda=0.73$, $h=0.7$, $n_s=0.95$, and $\sigma_8=0.82$.

2.1 Dark matter halo growth

We take the parametrized form for the mass growth of the dark matter halo given in equations (H1)-(H6) in Behroozi, Wechsler & Conroy (2013), which is tested against Bolshoi, Consuelo, and Multidark cosmological simulations.

2.2 Gas accretion

Gas accretion on to the galactic discs and subsequent star formation from the interstellar gas is the most important driver of the galaxy formation and evolution. In recent development of the hydrodynamical cosmological simulations, we have seen a significant revision of the traditional view about the physics of cosmic gas accretion.

The widely-used scenario for gas accretion on to forming galaxies, namely, the shock heating paradigm, assumes that the gas entering a dark matter halo is heated by shock waves to roughly virial temperature of the halo and subsequent radiative cooling induces the accretion of this gas to the inner parts where the galaxy grows (e.g. Rees & Ostriker 1977). In this picture, the gas accretes with the free-fall time if it cools rapidly while the accretion proceeds with the radiative cooling time when the cooling is not efficient. The cooling

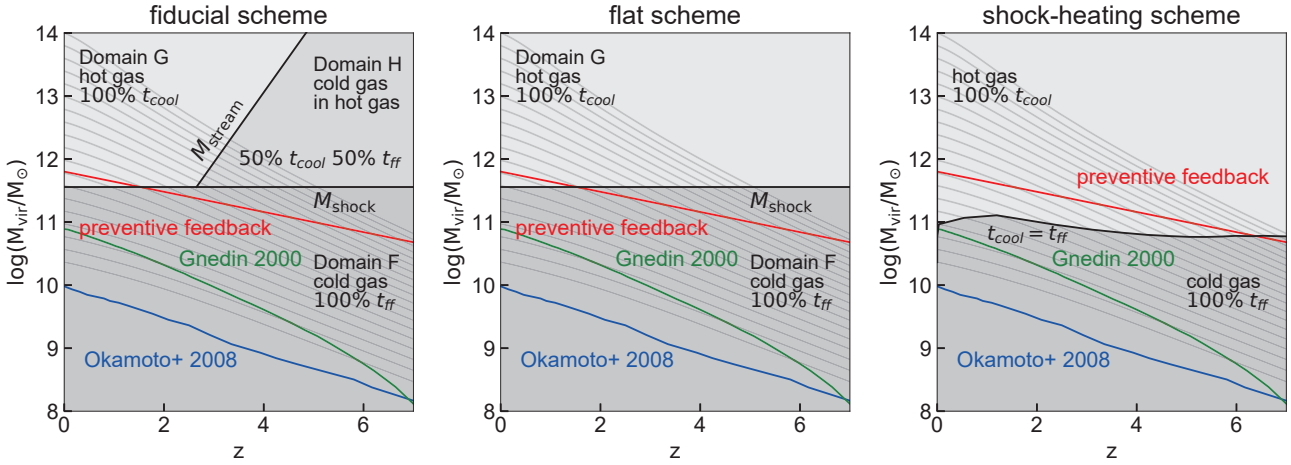


Figure 1. Three schemes for the gas accretion on to discs illustrated in the $(z - M_{\text{vir}})$ plane. For the fiducial scheme (left), three domains exist bordered by the shock mass, M_{shock} , and the stream mass, M_{stream} , as explained in the text. For the flat scheme (centre), the domain H is removed. The domains in the shock scheme (right) are separated by the border for which the cooling time is equal to the freefall time. In each domain, the halo gas accretes to the disc with the free-fall time (t_{ff}) or the radiative cooling time (t_{cool}) as indicated. The green line indicates the filtering mass proposed by Gnedin (2000), whereas the blue line indicates the virial mass below which the fraction of the baryon retained by the halo (relative to the cosmic baryon fraction) decreases to less than 90 percent due to UV background radiation from Okamoto, Gao & Theuns (2008). Red line indicates the characteristic mass for preventive feedback as explained in the text. Grey lines show the evolution track of each halo.

argument underlying this scenario succeeded in explaining the segregation of galaxies and galaxy clusters on the density-temperature plane (Blumenthal et al. 1984) and has constituted a backbone for many theoretical studies.

However, realistic simulations for hydrodynamical evolution of the primordial gas in the Λ CDM Universe (e.g. Fardal et al. 2001; Kereš et al. 2005; Dekel & Birnboim 2006; Ocvirk, Pichon & Teysier 2008; van de Voort & Schaye 2012; Nelson et al. 2013) found that the assumption of the stable shock underlying this picture is not always correct. The shock wave is unstable and no shock heating occurs in low mass halos. The unheated cold gas directly accretes to the inner parts in free-fall fashion in this case (e.g. Fardal et al. 2001; Birnboim & Dekel 2003; Kereš et al. 2005; Dekel & Birnboim 2006). In addition to this cold flow in low mass halos, high mass halos at high redshifts develop filaments of cold gas inflowing through the surrounding hot gas created by shocks (e.g. Dekel & Birnboim 2006; Ocvirk, Pichon & Teysier 2008; van de Voort & Schaye 2012; Nelson et al. 2013). The new picture, sometimes called the cold accretion scenario, has a large impact on our understanding of galaxy evolution. For example, it helps interpret the high abundance of actively star-forming galaxies at high redshifts (e.g. Cattaneo et al. 2006; Dekel et al. 2009). Lyman limit systems may be observational manifestations of the predicted cold streams (Fumagalli et al. 2011). The Ly α emitting filaments at high redshift observed by Martin et al. (2016) may provide a more direct example. Extending this picture to larger spatial scales, Overzier (2016) proposes that the transition from the cold accretion regime to the regime dominated by the hot intracluster gas in most massive halos marks the division between protoclusters and clusters of galaxies.

Noguchi (2018) demonstrated that the cold accretion scenario, combined with a chemical evolution model, reproduces the bimodality in the stellar abundance distributions of the Milky Way disc stars (for new observations, see Queiroz et al. (2020)). The transition from the early cold-mode to the late hot-mode gas accretion

sets the stage for two distinctive star formation episodes (see also Birnboim, Dekel & Neistein (2007)). The short period active star formation in early times produces metal-poor (i.e., deficient in Fe) stars with relatively enriched α -elements by the dominant action of type II supernovae. The late-time star formation proceeds slowly for a longer period allowing much iron enrichment by type Ia supernovae, leading to a metal-rich α -element-poor (low $[\alpha/\text{Fe}]$) population. Several cosmological simulations also show signs of such two-stage star formation in Milky Way mass galaxies (e.g. Hopkins et al. 2014; Grand et al. 2018), although details are often masked by other baryonic processes included. For galaxy morphology, the cold flow scenario was found to reproduce the relative dominance of thin discs, thick discs, and bulges in the present-day disc galaxies as a function of galaxy mass by associating the hot mode with thin disc formation and the cold mode with bulge and thick disc formation, respectively (Noguchi 2020). The observed galaxy-mass dependence of the mean age and the age spread of the bulge (Breda & Papaderos 2018; Breda et al. 2020) is also naturally explained by this model. We adopt this cold flow picture in our fiducial scheme described later and examine its essential role by comparing it with the accretion scheme based on the shock-heating picture.

2.3 Star formation

The accreted halo gas turns into interstellar gas in the galactic disc and serves as raw material for star formation. To calculate the star formation rate (SFR), we adopt the formulation by Blitz & Rosolowsky (2006) in which the SFR is essentially determined by the molecular gas content in the interstellar medium (ISM), with the molecular fraction in turn controlled by the disc midplane pressure. This treatment enables us to trace the evolution of the atomic and molecular contents separately. Those results are compared with the observation. Mass-loss associated with the evolution of massive stars is evaluated by assuming Chabrier IMF with lower and upper initial mass limits set to $1M_{\odot}$ and $100M_{\odot}$, respectively. The result-

ing mass fraction, $R = 0.44$ is returned to the ISM instantaneously (see Appendix A3).

2.4 Feedback

It is well established that the evolution of low-mass galaxies is strongly affected by the ejection of the ISM by supernovae on both observational and theoretical grounds (e.g. Dekel & Silk 1986; Mac Low & Ferrara 1999; Brooks et al. 2007; McQuinn, van Zee & Skillman 2019). It not only helps explain observations such as the mass-metallicity relation but also solves the over-production problem in the low galaxy mass domain inherent in the Λ CDM paradigm (see Bullock & Boylan-Kolchin (2017) for a review and Weinmann et al. (2012) for detailed discussion). We take the energy-driven feedback as the standard choice although the model with the momentum-driven feedback is also discussed.

Recent studies (Torrey et al. 2014; Somerville, Popping & Trager 2015, e.g.) suggest that supernova feedback alone cannot produce the masses of low-mass galaxies consistent with their metallicity. In order to realize the observed metallicity, those galaxies should be more massive than observed. Another type of feedback, called preventive feedback, was found to resolve this tension. Preventive feedback refers to the suppression of gas accretion on to halos or galactic discs by some mechanism(s). It can thus reduce the stellar mass of these galaxies without affecting metal enrichment driven by ejective feedback. Lu et al. (2017) point out the importance of preventive feedback in reproducing the galaxy stellar mass function and the mass-metallicity relation of the Milky Way satellites simultaneously. Several cosmological simulations (Angl ez-Alc azar et al. 2017; Christensen et al. 2016; Oppenheimer et al. 2010) show that this type of preventive feedback indeed occurs in galaxy formation although its detailed nature is not completely clarified. Candidate mechanisms include radio-mode feedback by active galactic nuclei (AGNs) (Kere s et al. 2009), heating from outflowing winds (Oppenheimer et al. 2010), and heating by ionizing radiation field (Efstathiou 1992; Gnedin 2000; Hoeft et al. 2006; Okamoto, Gao & Theuns 2008; Christensen et al. 2016). Preventive feedback can take two different forms. One is the reduction of the gas entering dark matter halos and another is the suppression of the gas supply from parent halos to galactic discs. Although this should be discriminated in the strict sense (e.g. Christensen et al. 2016), we include this process by reducing the accretion of the halo gas to the disc by a specified factor. We confirmed that the reduction of the gas entering the halo by the same factor gives indistinguishable results.

2.5 Gas recycling

Outflow of the interstellar gas is ubiquitously observed in star-forming galaxies with a large mass range and taken as a signature of ejective feedback. Because the outflow velocity attained by supernova feedback is typically less than several hundred kilometre per second (e.g. Chisholm et al. 2015), the outflowing gas may not leave the host galaxy entirely but a part of it may eventually fall back to the galaxy. Many numerical simulations demonstrate that such a fall-back actually occurs in actively star-forming galaxies (e.g. Christensen et al. 2016; Grand et al. 2019). This type of gas recycling has also been incorporated in the semi-analytic models (SAMs) (e.g. Croton et al. 2006; Henriques et al. 2013; White, Somerville & Ferguson 2015) and its effect on galaxy evolution has been intensively studied. These studies show that recycling affects not only global properties of galaxies but also their internal structures (e.g. Brook et al. 2012; Marasco, Fraternali & Binney 2012;

Grand et al. 2019). On the other hand, observational confirmation of gas recycling turned out to be inconclusive (see Fraternali & Pezzulli (2018) for a review). Although the infall of cold gas like galactic fountains is observed, several possibilities can be considered for its origin, including the cooling flow of the hot halo gas or the inflowing streams of unheated gas (cold-mode accretion). It is theoretically anticipated that the circulation of the ejected gas over much larger scales than the observed local fountains also takes place (e.g. Angl ez-Alc azar et al. 2017; Mitchell, Schaye & Bower 2020). Recent studies (e.g. Ford et al. 2014; Hasan et al. 2022) suggest that the recycling gas may be observed as quasar absorption lines (especially C_{IV}) but more work is required to firmly establish their connection. Considering these situations, we include this process simply by returning the ejected gas to the disc component with a specified timescale.

3 GAS ACCRETION SCHEMES AND MODEL FAMILIES

The first important question we must address is how the characteristics of gas accretion to discs influence the star forming activity in galaxies. To tackle this problem, we construct three kinds of model families employing different gas accretion schemes.

3.1 The fiducial scheme

The fiducial scheme assumes the existence of cold-mode accretion as revealed in recent cosmological simulations. Cosmological simulations and analytical consideration predict three different regimes for the properties of the gas distributed in the dark matter halos depending on the virial mass and redshift (e.g. Dekel & Birnboim 2006; Ocvirk, Pichon & Teyssier 2008). They are demarcated by two characteristic mass scales as shown in Figure 1 (left panel). One is the shock mass, M_{shock} , above which the halo gas develops a stable shock that heats the gas nearly to the virial temperature and the other is the stream mass, M_{stream} , below which part of the halo gas remains cold and is confined into narrow filaments that thread the smoothly distributed shock-heated gas. The latter mass scale is valid only for high redshifts.

The halo gas in Domain F is unheated and expected to accrete in free-fall to the inner region (the disc plane). In domain G, the gas heated to the virial temperature attains near hydrostatic equilibrium in the halo gravitational field and the radiative cooling induces cooling flow to the centre with the cooling timescale. The gas behaviour is not so clear in Domain H, where cold gas streams coexist with the surrounding shock-heated hot gas. They may behave independently and accrete with their own timescales or they may interact with each other leading to modification of accretion timescales. Because no detailed information is available, we assume that the cold and hot gases in Domain H accrete with the free-fall time and the radiative cooling time, respectively.

It is difficult to pin down the transition borders, namely M_{shock} and M_{stream} , which depend on various physical quantities of accreting gas with the gas metallicity being the most influential parameter. Cosmological simulations using different gas dynamical codes (e.g., SPH and AMR) show different results, with the Eulerian mesh codes (e.g., AMR) tending to suppress the cold fraction compared with the Lagrangian codes (e.g., SPH) (e.g. Nelson et al. 2013). We use the average of the results from several studies summarized in Figure 6 of Ocvirk, Pichon & Teyssier (2008), keeping in mind that the adopted prescription may suffer from ambiguity and affect quantitative detail of the result. Trial with several variations for the

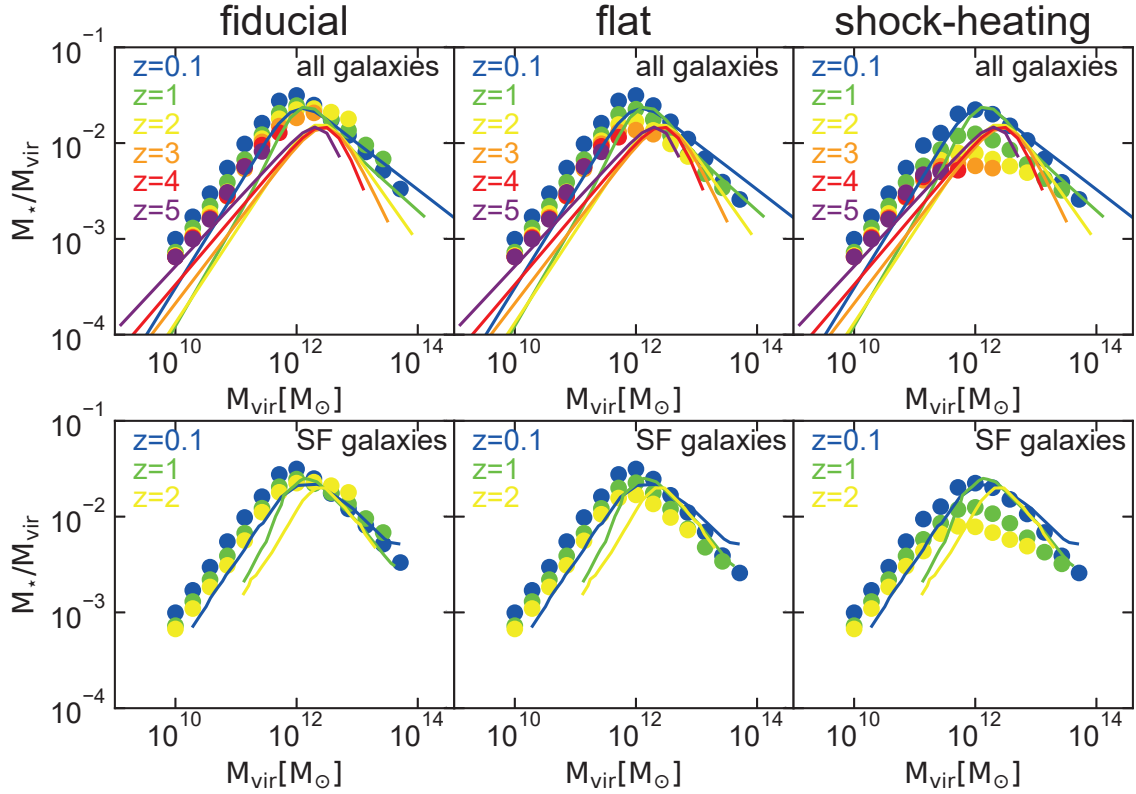


Figure 2. The ratio of the stellar mass to the halo virial mass as a function of the virial mass and redshift. Filled circles indicate the result for the schemes considered here. The upper panels compare the model with the results for all galaxies (quiescent and star forming) by Behroozi et al. (2019), whereas the lower panels compare the model with the result by Behroozi et al. (2019) only for star-forming galaxies.

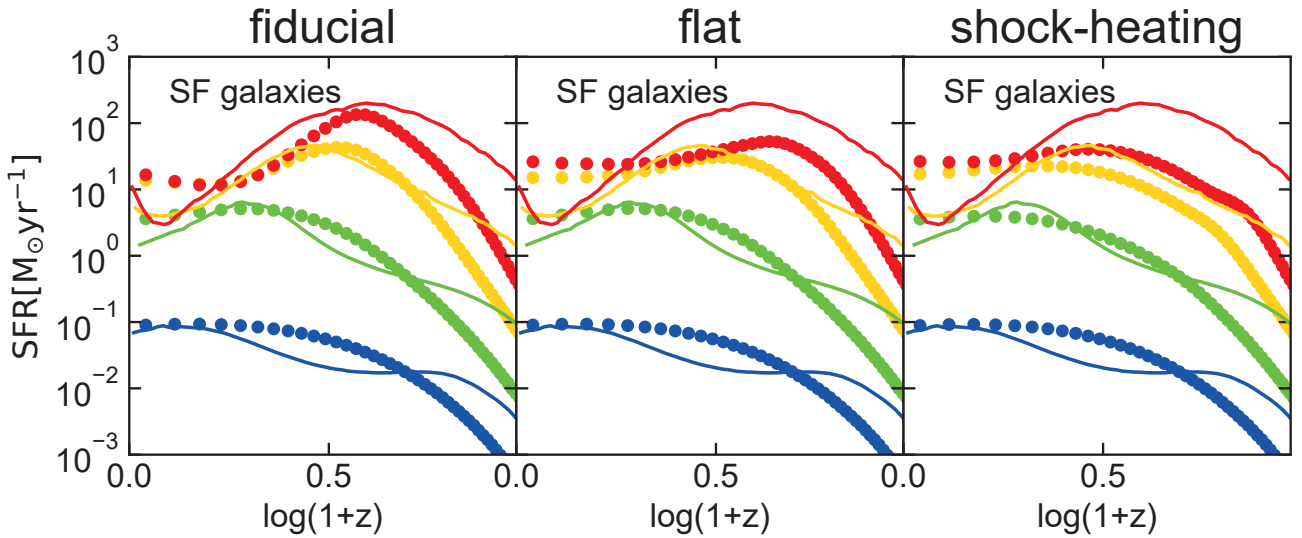


Figure 3. Star formation history as a function of the present halo virial mass. Filled circles with different colours denote SFR for different values for the present halo mass (blue: $10.5 < \log M_{\text{vir}} < 11.5$, green: $11.5 < \log M_{\text{vir}} < 12.5$, yellow: $12.5 < \log M_{\text{vir}} < 13.5$, red: $13.5 < \log M_{\text{vir}} < 14.5$). Solid lines show the results from Behroozi et al. (2019) for star-forming galaxies.

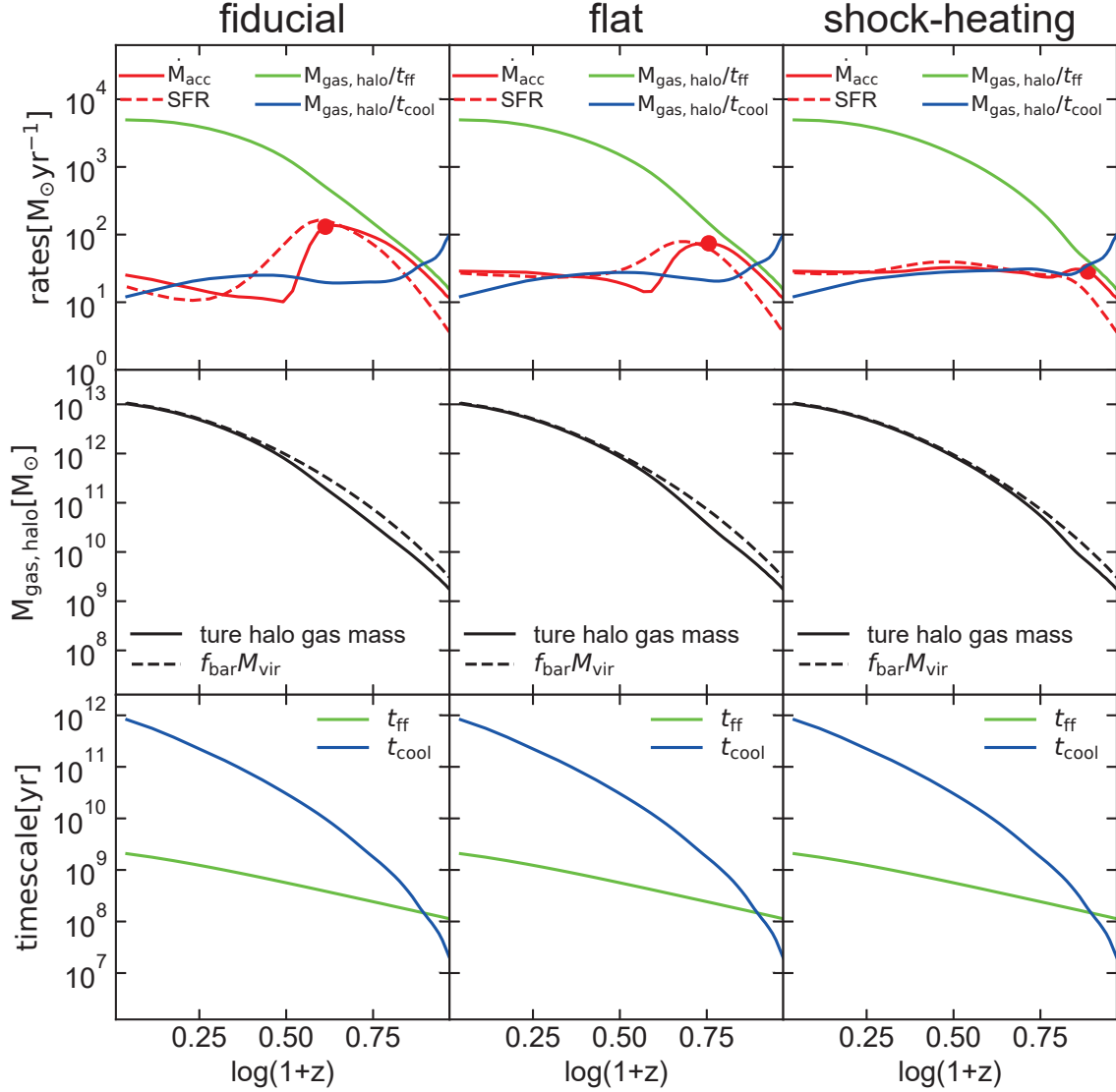


Figure 4. Evolution of gas accretion and star formation rates (upper panels), the mass of halo gas (middle panels), and the free-fall and radiative cooling times (lower panels) for the most massive halo with $M_{\text{vir}} = 10^{14} M_{\odot}$. Red solid and dashed lines in upper panels respectively show the accretion rates and SFR in the model in which only gas accretion is included. Circles on red solid lines indicate epochs when the halo enters the cooling flow regime (i.e., hot-mode accretion). Solid and dashed lines in middle panels are respectively the mass of the halo gas and the nominal mass $f_{\text{bar}} M_{\text{vir}}$, where $f_{\text{bar}} = 0.17$ is the adopted cosmic baryon fraction. Because the gas accretion continues to consume the halo gas reservoir, the actual halo mass is smaller than the latter, although their difference is small. Bottom panels, the same for all accretion schemes, indicate the radiative cooling time and the free-fall time. Green and blue lines in upper panels plot the actual halo gas mass divided by the free-fall and radiative cooling times, respectively.

transition borders, however, revealed that the qualitative nature of model evolution is conserved within plausible parameter ranges.

3.2 The flat scheme

Existence of Domain H is a distinguished characteristic of the cold mode accretion. In the previous work (Noguchi 2020), it was related to the formation of galactic bulges. The transition from the cold to hot modes corresponds to the quenching of star formation because

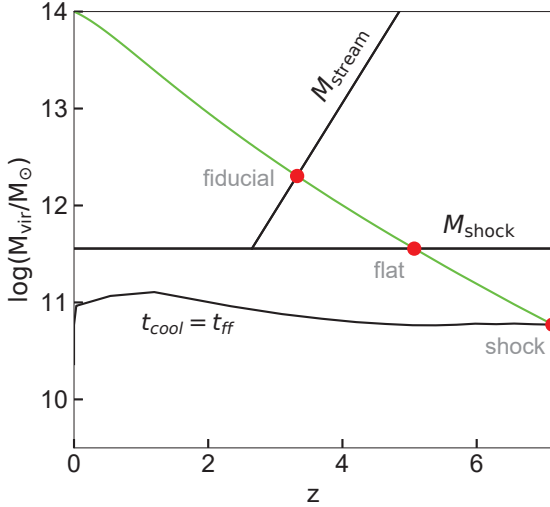


Figure 5. Comparison of transition from free-fall accretion to cooling-limited accretion in three different accretion schemes. The green curve indicates the trajectory of a halo with the present virial mass of $10^{14}M_{\odot}$. Red circles denote the transition for the scheme indicated.

the gas accretion slows down abruptly at this point. The reconstruction of galaxy assembly and SFH for the redshift range $z = 1 - 10$ by Behroozi et al. (2019) indicates increase of the quenching mass with redshift, though less steeply than the theoretical prediction of Dekel & Birnboim (2006). To elucidate the effect of Domain H on the galactic SFH, we run an artificial model family in which this domain is removed (middle panel in Figure 1).

3.3 The shock-heating scheme

The shock heating picture has been routinely assumed in many theoretical studies of galaxy formation. It is interesting to see the difference between the star formation history derived under the fiducial scheme and this picture. There are two domains in this scheme separated by the equality of the radiative cooling time and the free-fall time (Figure 1, right panel). When the gas cools with timescale shorter than the free-fall time, it is made to accrete with the free-fall time. Otherwise, the gas is assumed to accrete with the cooling timescale.

For each accretion scheme, we run a series of galaxy models with the present halo virial masses varied in the range $10^{10.36}M_{\odot} \leq M_{\text{vir},0} \leq 10^{14}M_{\odot}$. This upper mass limit roughly corresponds to the halo mass inferred for the most massive (disc) galaxies with the stellar mass $\sim 10^{11.5}M_{\odot}$ on the basis of the abundance matching analysis (e.g. Moster, Naab & White 2013; Rodríguez-Puebla et al. 2015; Behroozi et al. 2019). The lower mass limit corresponds to the stellar mass of $\sim 10^7M_{\odot}$, below which the observational material becomes sparse. Grey lines in Figure 1 show the evolution of each halo, illustrating how it goes through different regimes of gas accretion as it grows in mass. Because no galaxy merger is considered in this study, the present models are regarded as mainly describing the evolution of galaxies whose growth rates are inflow dominated.

It is remarked here that the schemes illustrated in Figure 1

may need some modification. As seen later, preventive feedback which acts to reduce gas accretion to the galactic disc, is found to be important especially for low mass halos. The red line in each panel of Figure 1 indicates the critical halo mass assumed in this study for which this effect starts to be active. Although the specific mechanism responsible for this process is not clear, previous studies suggest that it affects a wider range of mass than the ionization by background radiative fields. For comparison, we also plot the ‘filtering mass’ by Gnedin (2000) and the 90% suppression line by Okamoto, Gao & Theuns (2008) as a typical estimate for the radiative effect. Preventive feedback, either on to discs or on to halos, may thus significantly alter the picture solely based on the cooling argument (and assumption of a universal cosmic baryon fraction). We revisit this issue later.

4 COMPARISON BETWEEN DIFFERENT ACCRETION SCHEMES

We first examine and compare the behaviours of the models for the three different gas accretion schemes. We also compare the result with available observational data. In this section, the parameters describing ejective feedback, preventive feedback, and gas recycling are set to default values as given in Appendix.

4.1 Star formation history

Figure 2 shows the stellar-to-halo mass ratio as a function of the halo virial mass for different redshifts. The halo mass here denotes the mass at each redshift. The empirical analysis by Behroozi et al. (2019) using the abundance matching method shows no significant difference between the star forming galaxies and all galaxies including quiescent galaxies. At the present epoch ($z \sim 0$), all schemes give similar results approximately agreeing with the result by Behroozi et al. (2019) and other observational studies. Moving to higher redshifts ($z > 2$), the shock-heating scheme progressively underproduces stars especially for more massive halos. This is due to earlier transition of massive halos to the hot-mode gas accretion and associated weakening of star formation. The predicted redshift dependence seems to be significantly stronger than the observationally inferred one even if we make allowance for the possible systematic deviation as suggested by the small (~ 0.3 dex) overproduction in the low mass domain ($M_{\text{vir}} < 10^{12}M_{\odot}$) common to all three schemes.

Figure 3 shows the star formation history (SFH) for different values of the present halo masses. It is seen that the fiducial scheme captures several key features of the observed SFHs. Namely, the SFR in halos with larger present masses attains the peak at earlier epochs and declines more drastically after the peak. The halos in the lowest mass bin (the blue line) show monotonically increasing SFR. Notable discrepancy is seen at $z > 2$ where the models underpredict SFR compared with the observation. This may indicate that the adopted feedback is too strong. However, the discrepancy for most massive halos appears also in absence of feedback as seen later in section 5. We discuss possible reasons for this discrepancy there.

The flat scheme is unable to reproduce this mass dependent behaviour. This indicates that the existence of the domain H defined by the existence of cold gas streams contributes much in producing the observed mass dependent SFH, especially the early drastic ‘quenching’ in massive halos. The shock-heating scheme also fails due to the same reason. It is interesting that Behroozi et al. (2019) compare

their results for the quenching fraction (their Figure 30) to the prediction of [Dekel & Birnboim \(2006\)](#) cold accretion model and find rough agreement, i.e., the domain for star forming galaxies extends to higher halo masses at higher redshifts. This is in line with the present result showing the importance of the cold-mode accretion of gas filaments penetrating through the surrounding shock-heated halo gas although some other mass-dependent process (e.g. mergers) might bring about a similar effect.

Differences in SFHs in the three schemes displayed in Figure 3 appear in high-mass domain with $\log M_{\text{vir}} [M_{\odot}] > 12.5$, where accretion processes are different. Specifically, massive galaxies in the fiducial scheme experience peak SFR in earlier epochs and larger drop in SFR after the peak than those in the flat scheme while massive galaxies in the shock heating scheme show no peak. Figure 4 is meant to clarify the origin of these various SFHs going back to the difference in the prescribed accretion recipes. Top panels show the gas accretion rates (red solid lines) and SFRs (red dotted lines) for $\log M_{\text{vir}} [M_{\odot}] = 14$ in the three accretion schemes. For aid in analysis, middle panels show masses of the halo gas and bottom panels plot the radiative cooling time (blue) and the free-fall time (green) for the halo gas. We here turn off supernova feedbacks, gas recycling and preventive feedback to explore more directly how the halo gas mass and the two timescales eventually control the SFR under accretion-driven situation.

Top panels indicate that SFRs essentially follow gas accretion rates with small time delay. Gas accretion rates in turn can be approximated by the amount of halo gas divided by the accretion timescales. Middle panels show that the mass of halo gas (solid) is almost the same in the three schemes. Therefore, the differences in SFHs should originate mostly in those in accretion timescales. Green and blue lines in upper panels are the 'accretion rates' calculated by dividing the true halo gas mass respectively by the free-fall time and radiative cooling times. These are again similar in the three schemes reflecting the similarity in the halo gas mass.

The key for interpreting different SFHs lies in how the transition from the cold-mode accretion to the hot-mode accretion occurs. At the transition, the accretion timescale is switched from the free-fall time to the radiative cooling time. Figure 5 compares this transition for three accretion schemes. In the shock-heating scheme, the transition occurs exactly when the cooling time overshoots the free-fall time, but in the other two schemes it occurs when the initial cold-accretion phase ends, which is later than the equality of two timescales. Instability of shocks in the flat scheme delays the transition compared with that in the shock-heating scheme. Existence of cold streams in high-mass halos further retards the transition in the fiducial scheme. Upper panels in Figure 4 overplot the transition epoch by red circles on the accretion rate curves. It is seen that the actual accretion rates (red lines) follow closely the green lines before this transition epoch but they deviate and approach to blue lines after that. Comparison of three accretion schemes thus reveals that the difference in the accretion history comes from the difference in the transition epoch. Moving from the shock-heating to flat to fiducial schemes, the transition epoch moves progressively to more recent epochs and therefore the drop in accretion rate gets larger because of larger difference in timescales at transition. This explains why the peak SFR occurs latest and the decrement in SFR after the peak is the largest for the fiducial scheme as shown in Figure 3.

The SFHs such as plotted in Figure 3 will contain all information about the star formation activity in galaxies if accurately derived over the whole mass range. However, halo masses in the empirical approach are not obtained for each sample galaxy but

derived statistically from abundance matching. On the other hand, it is not easy either to measure the halo masses for individual galaxies more directly, for example, from satellite kinematics (e.g. [More et al. 2011](#)) or weak gravitational lensing (e.g. [Mandelbaum et al. 2006](#)). Any derived SFHs as a function of halo mass could thus be subject to uncertainty even if SFRs are obtained precisely. We examine in the next section the dependence of star formation activity on the stellar mass, which is more directly assessed than the halo mass in general.

4.2 Main sequence evolution

The correlations between star formation properties and galaxy stellar masses have been intensively examined in previous studies. Among various scaling relations, the star formation main sequence (MS) of galaxies, i.e., the SFR- M_{\star} relation, provides useful information on how galaxies with different masses formed stars over the cosmic time (e.g. [Whitaker et al. 2014](#); [Johnston et al. 2015](#); [Schreiber et al. 2015](#); [Kurczynski et al. 2016](#); [Tomczak et al. 2016](#); [Schreiber et al. 2017](#); [Popesso et al. 2019](#); [Corcho-Caballero, Ascasibar & López-Sánchez 2020](#); [Khusanova et al. 2021](#)) and serves as an independent constraint on theoretical modelling (e.g. [Feldmann 2020](#)).

Figure 6 compares the SFR and sSFR predicted by the models with the observational data. It is seen that the fiducial scheme reproduces several important features at least qualitatively. Regarding the SFR- M_{\star} relation (top panels), it gives the SFR that increases almost linearly with the stellar mass for the low-mass range, with normalization increasing with redshift. The relation at higher masses bends in progressively larger degree for lower redshifts. This behaviour agrees with the observational results about the redshift evolution of the normalization of the star formation MS and the turn-over in the high mass range (e.g. [Whitaker et al. 2014](#); [Tomczak et al. 2016](#)). Both the flat and shock-heating schemes give a reverse trend at high masses with smaller bending at lower redshifts. The middle panels plot the sSFR as a function of the stellar mass. The fiducial scheme shows nearly horizontal relation for low masses and increasingly steeper decline at high masses toward lower redshifts, agreeing with the observational analysis. The other two schemes fail to reproduce the observed trend. Although we take here the observation by [Whitaker et al. \(2014\)](#) as a typical example, other observational studies also reveal similar trends (e.g. [Schreiber et al. 2015](#); [Tomczak et al. 2016](#); [Rodríguez-Puebla et al. 2020](#)).

Difference in the turn-over at high masses in different accretion schemes is directly related to difference in the SFHs. In order to clarify this point, Figure 7 overplots the trajectory of evolving model galaxies on the SFR- M_{\star} relation. It is evident that large flattening at high mass end in the fiducial scheme is caused by strong drop in the SFR when the gas accretion is switched from the cold mode (solid curve) to the hot mode (dashed curve) in massive halos with $M_{\text{vir}} > 10^{13} M_{\odot}$. During the hot-mode phase, M_{\star} increases by only 0.2 dex while SFR decreases by almost 1 dex in the most massive halo. The decrement in SFR is larger for more massive halos that move down on more right sides of the SFR- M_{\star} diagram, leading to the fan shape pattern of redshift sequence in the fiducial scheme. High-mass end of the main-sequence is related to the hot mode accretion also in the flat and shock-heating schemes. In these cases, however, the decrease in SFR is milder and the stellar mass increases with almost constant SFR. Namely, the galaxy moves rightward nearly horizontally in the diagram. This means that the main sequence itself moves rightward. Combination of this movement and the weak turn-

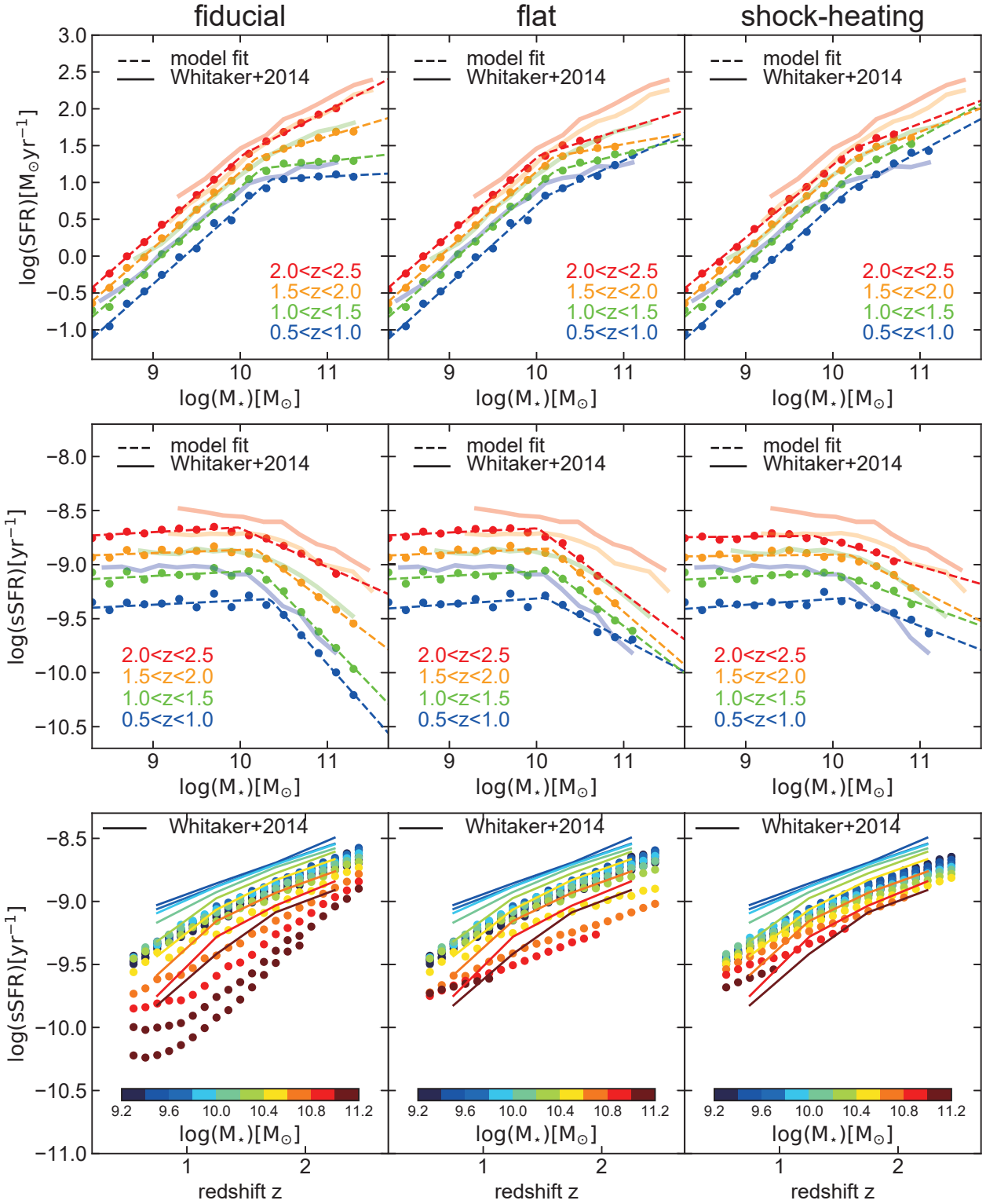


Figure 6. Top panels: Star formation rate as a function of the stellar mass for different redshift bins. Filled circles indicate the model result with the dashed lines showing the least square fit of the model result by broken power law. The solid broad lines indicate the result for star-forming galaxies by Whitaker et al. (2014). Middle panels: Same as the top panels but for the specific star formation rate. Bottom panels: Specific star formation rate as a function of redshift for different stellar mass bins. The solid lines are corresponding curves obtained by Whitaker et al. (2014) using UV+IR data.

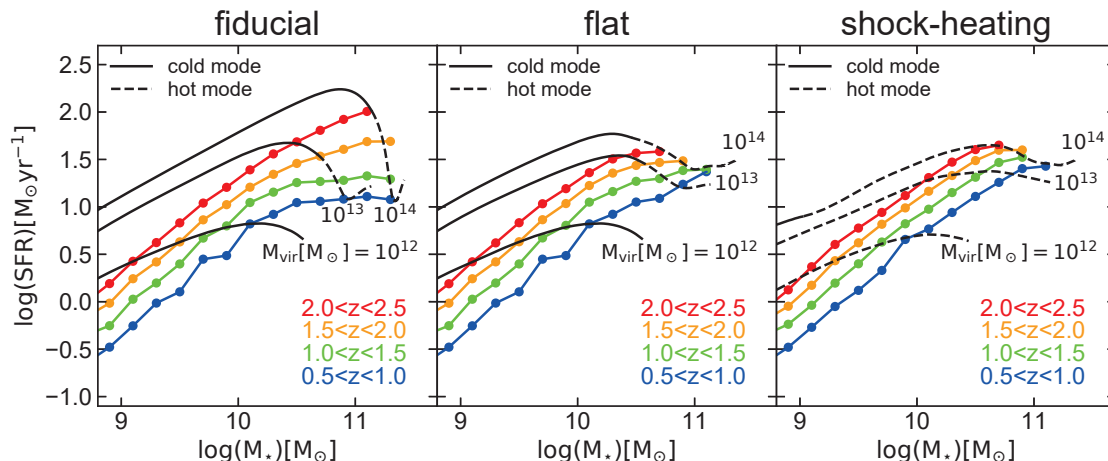


Figure 7. Evolution trajectory of model galaxies overplotted on the model main sequence. The main sequence is the same as the one plotted in Figure 6. Trajectories are from top to bottom for the halos with $\log M_{\text{vir}} = 14, 13, 12$, respectively. Solid and dashed parts denote the period of cold-mode and hot mode accretion, respectively.

over at high stellar masses at each redshift makes a configuration of the redshift sequence converging to higher stellar masses.

There has been much debate about the existence of the turn-over at high masses (e.g. Santini et al. 2017; Popesso et al. 2019). Speagle et al. (2014) argue that the MS is nearly linear and its slope and normalization decrease toward recent epochs, dismissing the existence of turn-over. The slope at the high mass domain likely depends on the selection criteria for star-forming galaxies (Johnston et al. 2015). Galaxy morphology is also suggested to affect the high-mass behaviour of the MS. For example, including galaxies with dominant bulge components, usually characterized by smaller sSFR compared with the bulgeless galaxies of similar masses, was found to create strongly downward bending at high masses as reported by Cook et al. (2020). Teimoorinia, Bluck & Ellison (2016) also suggest close empirical relationship between the bulge mass (or the bulge-to-total mass ratio) and the star formation activity. There is also a possibility that the star formation properties and the main sequence characteristics depend on the galactic environments (e.g. Elbaz et al. 2007; Gnedin & Kravtsov 2011; Zeimann et al. 2013; Ji et al. 2018; Noirot et al. 2018; Nantais et al. 2020; Old et al. 2020). We return to these issues later in Discussion.

The bottom panels of Figure 6 show the redshift evolution of the sSFR for different stellar masses. The fiducial scheme produces steeper decline of sSFR with time for more massive galaxies in qualitative agreement with data, whereas other two schemes show opposite trends in contrary to observations. This is a reflection of different turn-over behaviours seen in top panels. Absolute value of sSFR is underpredicted commonly in all accretion schemes for $\log M_{\star} [M_{\odot}] < 10.4$. For $10.4 < \log M_{\star} [M_{\odot}] < 11.0$, the fiducial scheme gives closer match to the observational data than other schemes. Finally, for $11.0 < \log M_{\star} [M_{\odot}]$, the fiducial scheme exhibits smaller sSFR than other schemes.

The present result highlights the importance of gas accretion process in determining the shape and evolution of the star formation MS. Especially, the shock-heating scheme seems to be incapable of explaining the qualitative behaviour of turn-over in the star formation main sequence claimed by several observational works. This result agrees with that from several theoretical studies. The semi-analytic models adopting the shock-heating paradigm for the halo

gas (e.g. Mitchell et al. 2014; Brennan et al. 2015; Henriques et al. 2015; Somerville, Popping & Trager 2015; White, Somerville & Ferguson 2015; Guo et al. 2016) tend to produce the sSFR- M_{\star} relation that stays almost flat or even rises more steeply with the stellar mass toward more recent epoch, being completely opposite to the observation. The disc galaxy evolution models by Dutton, van den Bosch & Dekel (2010) and Lapi et al. (2020) assuming the shock heating also produce the SFR- M_{\star} relation similar to these models. On the other hand, the model by Bouché et al. (2010) taking into account the cold-mode gas accretion produces the SFR- M_{\star} relation that evolves only in the normalization. Cosmological simulations (e.g. Hopkins et al. 2014; Vogelsberger et al. 2014; Furlong et al. 2015; Sparre et al. 2015; Schaye et al. 2015; Donnari et al. 2019; Scholz-Díaz, Sánchez Almeida & Dalla Vecchia 2021) tend to produce turn-over at high masses and show agreement with the observation to some extent but its reason remains unclear. One possibility is that these simulations, treating gas processes more directly, automatically contain the cold-mode phase of gas accretion.

It should be noted that the main sequence turn-over may arise from other reason than specific feature of gas accretion. Generally, any feedback process operating preferentially on massive halos would produce a qualitatively similar effect. For example, the feedback from AGNs (when included) may contribute to the main sequence turn-over as argued in (Donnari et al. 2019). In this specific case, AGN feedback should closely follow star formation. Quasar-mode feedback may be thus promising, though the coupling of feedback energy and the halo gas should be clarified to confirm its feasibility.

We focused so far on the star formation activity represented by the SFR and the sSFR. We here examine the growth of stellar mass for different halo masses. Figure 8 illustrates the stellar mass build-up in terms of the absolute mass (top row) and the fractional mass (middle and bottom rows). It is clear that the fiducial scheme explains the so-called downsizing that more massive galaxies grow faster. Indeed, downsizing behaviour is already hinted in SFHs shown in Figure 3. This trend is more clearly shown by the fractional mass growth plotted in the middle and bottom rows. In the flat and shock-heating schemes, the galaxies with different masses grow almost in concert. The grey shading in the bottom panels indi-

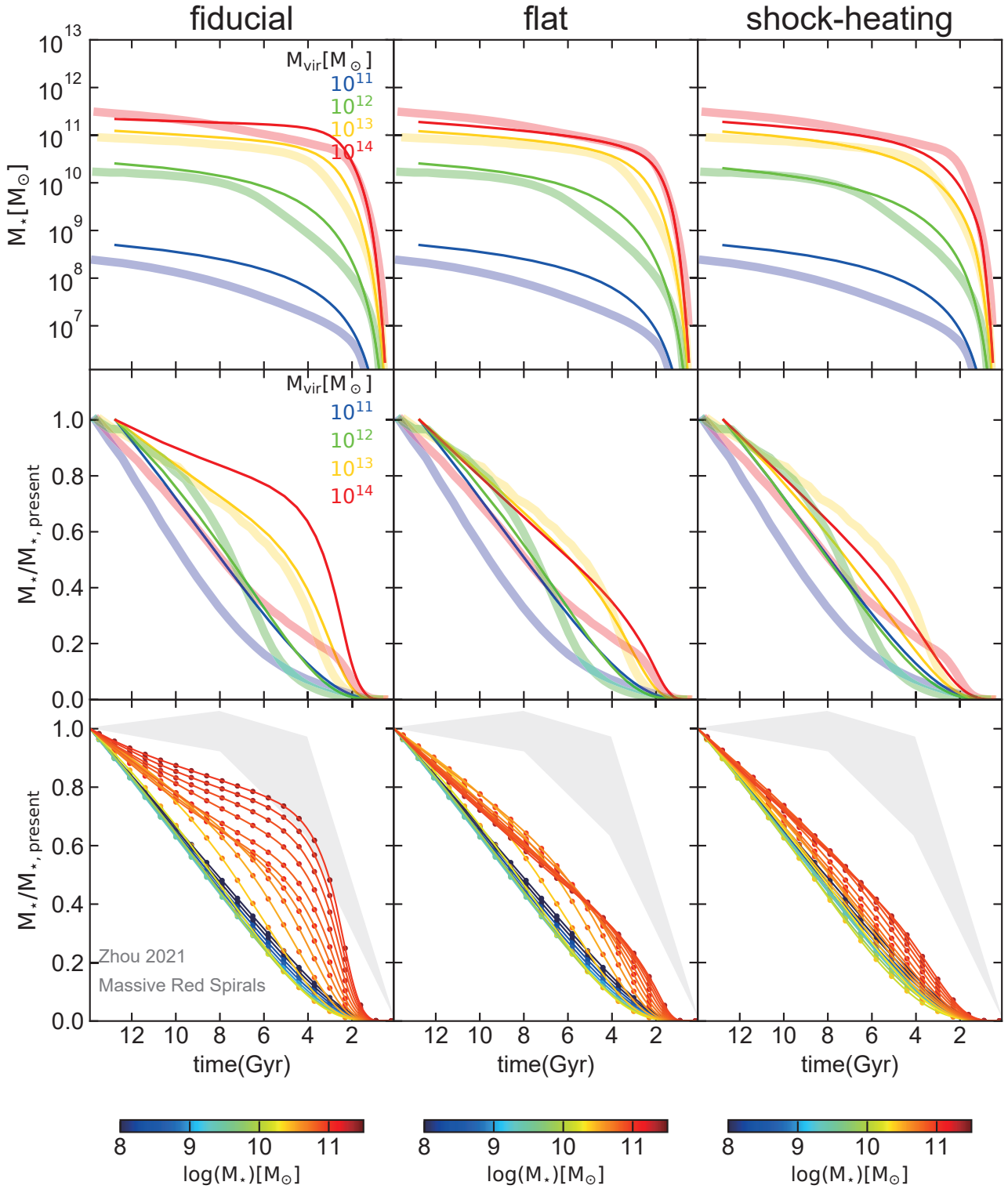


Figure 8. Stellar mass growth history for different masses. Top row: Thin solid lines indicate the time evolution of the stellar mass for different halo masses. Red, yellow, green, and blue indicate the present virial masses of 10^{14} , 10^{13} , 10^{12} and $10^{11}M_{\odot}$, respectively. Broad shaded lines show the result by Behroozi et al. (2019) for all galaxies with the corresponding mass ranges. Middle row: same as top row but plotting the normalized stellar mass against the cosmological time. Bottom row: Same as the middle row but as a function of the stellar mass at the present epoch. The shaded region illustrates the inferred evolution for red massive spiral galaxies by Zhou et al. (2021) with the stellar masses $10^{10.5} - 10^{11.5}M_{\odot}$.

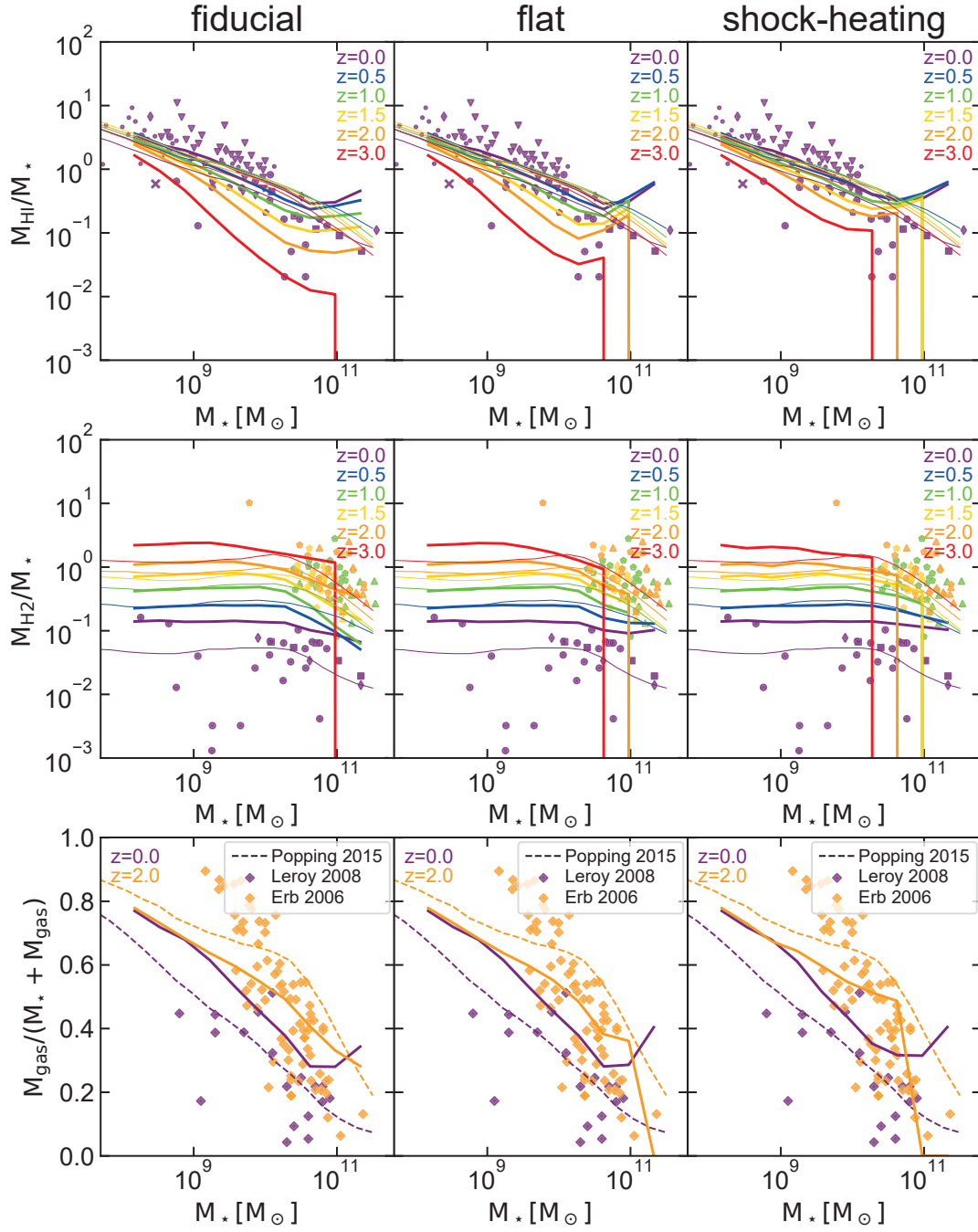


Figure 9. The cold gas contents as a function of stellar mass obtained in the present study (thick solid lines) and the analysis by Popping, Behroozi & Peebles (2015) (thin solid lines in the upper and middle panels and dashed lines in the bottom panels) for different redshift bins with the width of 0.2 centered on the indicated redshift. Top panels: The mass ratio of the atomic hydrogen and stars. Observations from various literatures are indicated by symbols as follows. squares: Saintonge et al. (2011), diamonds: Bothwell, Kennicutt & Lee (2009), circles: Leroy et al. (2008), dots: McGaugh (2012), pentagons: Boselli et al. (2014), inverted triangles: Bothwell et al. (2014), x: Zhang et al. (2012). Middle panels: same as top panels but for the molecular gas. Observations from various literatures are indicated by symbols as follows. squares: Saintonge et al. (2011), diamonds: Bothwell, Kennicutt & Lee (2009), circles: Leroy et al. (2008), triangles: Genzel et al. (2010), pentagons: Tacconi et al. (2013). Bottom panels: The mass fraction of the total gas (atomic+molecular) relative to the total baryonic (gas + stars) content as a function of the stellar mass for $z = 0$ (purple) and $z = 2$ (orange). Observational values for $z = 0$ are from direct measurements by Leroy et al. (2008). Those for $z = 2$ are the values from Erb et al. (2006) who estimated the total gas mass from star formation rates.

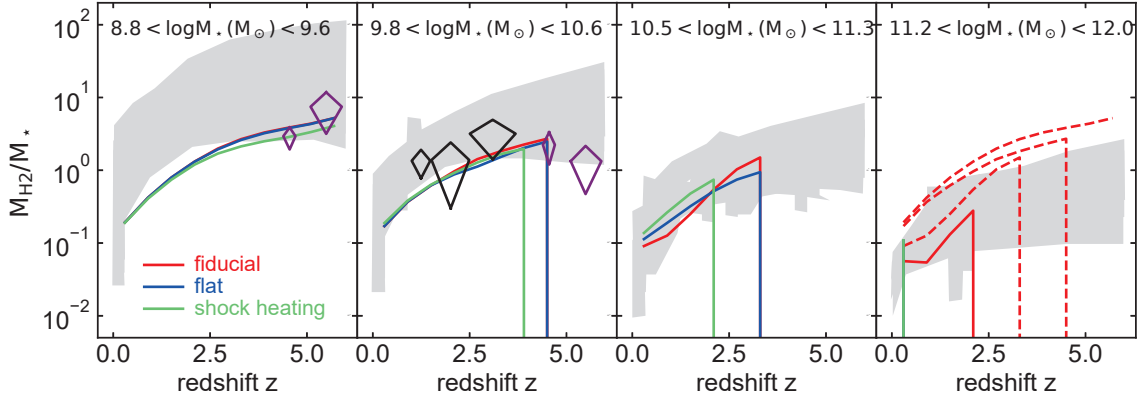


Figure 10. Evolution of the mass ratio of the cold molecular gas and the stellar content for different stellar mass bins in three accretion schemes. Gray shaded regions summarise the observational data from the literature including Scoville et al. (2017), Tacconi et al. (2018), and Liu et al. (2019). Diamonds indicate the values and their errors reported by Dessauges-Zavadsky et al. (2020) for the ALPINE [C II]-detected nonmerger galaxies (purple) and the CO-detected galaxies from their compilation (black), respectively. Three dashed lines in the rightmost panel repeat the less massive models in the fiducial scheme shown in left panels to illustrate the mass dependence of the molecular content.

icates the observed range derived by Zhou et al. (2021) for massive red spirals. The fiducial scheme gives better reproduction than the other two schemes for the high-mass range. The reason is that the prolonged period of cold-accretion in this scheme allows more halo gas to accrete to the disc at early times ($z > 2$) and raises SFR above those in other two schemes as illustrated in Figure 4. It nevertheless fails in matching the observation for $t > 8$ Gyr. This arises from the upturn in SFR for massive halos at $z < 0.5$ seen in Figure 3 because it brings about significant stellar mass growth in recent epochs and makes early quenching impossible. This discrepancy could be erased by including, for example, AGN radio-mode feedback which likely operates for low gas accretion rate in the hot-mode phase.

4.3 Evolution of cold gas contents

Star formation rates in galaxies are controlled by the amount of cold gas that serves as raw material for star formation and the timescale (depletion time) for gas consumption. The amount of gas in turn could be determined by several factors including the rate of gas accretion, ejection or removal rate of ISM, and recycling efficiency of ejected ISM. Confrontation of the model prediction for the evolution of gas contents with observational data therefore helps judge importance of each factor in galactic star formation. Gaseous content of the cold interstellar medium is classified into atomic hydrogens (HI) and molecular hydrogens (H_2). While the molecular gas is probed to high redshifts up to $z = 2 \sim 3$ thanks to the detection of CO lines, the observation of atomic component is currently restricted to the local Universe, $z < \sim 0.2$, due to the bandshift effect of 21 cm emission lines. Recent large surveys (e.g., BIMA SONG, HERACLES, COLD GASS) have revealed that the molecular masses relative to the stellar masses generally increase toward earlier cosmological epochs (e.g. Helfer et al. 2003; Leroy et al. 2008; Genzel et al. 2010; Saintonge et al. 2011; Tacconi et al. 2013). Census for the atomic gas in the local Universe (e.g., ALFALFA, THINGS, GASS) consistently indicates a decreasing HI mass fraction toward increasing stellar masses (e.g. Giovanelli et al. 2005; Walter et al. 2008; Catinella et al. 2010).

Figure 9 compares the model result (thick solid lines) with the

currently available observational data (symbols). Redshift is colour-coded as indicated. The top panels show the mass ratio of the atomic hydrogen and the stellar content as a function of the stellar mass. At $z = 0$, all the schemes give similar trends in broad agreement (a factor of ~ 2) with the observation. As we move to higher redshifts, the difference between the three schemes becomes clearer, with the fiducial scheme showing the largest decrease. The thin lines indicate the empirical result obtained by Popping, Behroozi & Peebles (2015), which shows very little evolution with redshift. The simulation by Davé et al. (2013) also suggests little evolution in HI content. It is noted that the result by Popping, Behroozi & Peebles (2015) was obtained indirectly from the observed SFR by using the abundance matching technique combined with the locally established star formation law and the result by Davé et al. (2013) is also based on several assumptions in calculating HI fraction. If nevertheless these theoretical studies turn out to give better match to future observations, the shock-heating scheme might seem the most promising. There is a caveat here, however. Stronger decrease in HI content to higher redshifts for the fiducial scheme than in other schemes may have partly resulted from more active cold accretion that produced discs with richer gas content. Gas richness (i.e., higher surface densities) in discs means a relatively higher fraction of H_2 in the disc and therefore poorer HI content. Another possible factor influencing gas contents is their spatial distribution. In actual galaxies, H_2 and HI are spatially decoupled, with the former more concentrated to galactic centers (e.g. Young & Scoville 1991). The model assumes that two components have the same scalelength corresponding to the halo spin parameter λ of 0.06, which gives disc radii more relevant to the molecular component. Increasing λ to 0.08 as a compromise between two components significantly lifts up HI content relatively to H_2 due to resulting lower gas densities. It also diminishes difference in redshift dependence between different schemes, weakening apparent advantage of the shock-heating scheme. Argument relying on the spin parameter is admittedly rough but this result suggests a promising avenue to resolve the difficulty shown here.

Middle panels of Figure 9 show the mass ratio of the molecular hydrogen. Compared with HI, all the schemes show much weaker mass-dependence with only the normalization increasing with red-

shift. Weak mass dependence agrees with the observed trend. The observational data and the empirical model by [Popping, Behroozi & Peeples \(2015\)](#) (thin lines) indicate the mass ratio at $z = 2 - 3$ larger than the local value by more than ~ 1.5 dex. All schemes give good match to this result but tend to overpredict M_{H_2}/M_\star up to ~ 1 dex at $z = 0$. This likely originates in overabundance in ISM gas in model galaxies (especially massive ones) at recent epoch. Increasing gas ejection artificially by 1 dex for $z < 0.5$ leads to lower molecular content and better agreement at $z=0$. This modification also helps erase turn-up of model SFRs at $z < 0.5$ in massive halos seen in Figure 3 for the fiducial scheme, and improve agreement with the observation. Although we boosted here the ejection rate by supernova feedback artificially, more promising alternative mechanism to operate is radio-mode AGN feedback that likely acts preferentially for massive halos (Domain G of the fiducial scheme) at low redshifts.

Bottom panels of Figure 9 show the mass fraction of the total gas including atomic and molecular hydrogen. The three schemes all show an increasing fraction toward smaller stellar masses, with the value at fixed mass at $z = 2$ larger than in the local Universe. These trends agree qualitatively with the observation but the latter suggests larger ratios and steeper mass dependence at $z = 2$ whereas the ratios are smaller at $z = 0$. The dashed lines indicate the result of the analysis performed by [Popping, Behroozi & Peeples \(2015\)](#). Their result shows larger redshift dependence than our models, though the slope of mass dependence is similar. The discrepancy of the fiducial scheme and observation can be partly relieved by using combination of the large spin parameter and boosting of gas ejection discussed above. Larger spins contribute to boost HI content at $z = 2$ without affecting the molecular content, leading to larger gas-to-stellar ratio. Applied boosting reduces H_2 content at $z = 0$ reducing gas fraction. Two effect combine to produce larger redshift evolution in closer agreement with the observational data. Exploring evolution of two gas components consistently requires knowledge of density profiles of those components and reliable information about angular momentum distribution of infalling gas, which control disc sizes. Radio mode AGN feedback is believed to operate in low efficiency accretion to massive black holes provided by the hot-mode accretion ([Fabian 2012](#), e.g.). Including growth of black holes is necessary to treat this process properly. We defer such investigation to future study.

Recent observations of the molecular gas can reach $z > 5$. Additional analysis was carried out of the evolution of the molecular gas over large redshift range. The result is shown in Figure 10 for different stellar mass bins. This figure gives the essentially same information as the middle panels of Figure 10 but now shows the redshift dependence to earlier cosmological epochs. The observations suggest the ratio of the molecular mass to the stellar mass increasing with redshift up to $z > 5$ for all mass bins and larger ratios for lower mass galaxies at the fixed redshift. The three schemes considered here show a qualitatively similar behaviour to the observation although the discrepancy can reach ~ 1 dex at the lowest mass bin, where the three schemes give nearly identical evolution. Although the fiducial scheme cannot reproduce every detail of the observational result, it predicts strong evolution of the molecular content in agreement with the observation. These analyses also suggest that the improvement in the observational data for galactic gas contents (especially the redshift evolution of the atomic gas) is needed to further constrain the models examined here. The data expected to be obtained by the newest instruments such as Atacama Large Millimeter Array (ALMA) and Square Kilometre Array (SKA) will serve as a powerful constraint on theoretical models.

5 ROLES OF FEEDBACK AND GAS RECYCLING

The discussion above highlights the potential importance of the cold-mode accretion especially for massive galaxies. The cold-mode proceeding with free-fall time delivers halo gas to discs rapidly supporting high SFR. In the fiducial scheme, this phase lasts longer than in other two cases until the epoch when the radiative cooling time becomes far-longer (by ~ 1 dex) than the free-fall time. When the accretion is switched to hot cooling-limited mode, the accretion rate and therefore SFR drops drastically by ~ 1 dex (see Figure 4), reproducing strong quenching observed in massive galaxies (Figure 3) and inducing large main-sequence turn-over at high-mass end (Figure 7).

Here we examine the role of other physical processes (preventive feedback, ejective feedback, and ISM gas recycling) which could modulate the evolution driven by gas accretion. For the reference model in this practice, we adopt a model in which only gas accretion of the fiducial scheme is included, which we call the accretion-only model. We perform three kinds of modelling by adding ejective feedback, ejective feedback plus gas recycling, and preventive feedback separately to the accretion-only model. By comparing each type of model with the accretion-only model, we aim to isolate the effect of each process added. In the following, we restrict the gas accretion to the fiducial scheme and the parameters for each added process are default values unless otherwise stated. We can reverse this procedure by removing each process from the full model. This was done and the conclusions about the respective role of those processes remain the same.

Figure 11 is similar to Figure 2 but indicates the effect of each process on the stellar-to-halo mass ratio. It is seen that the accretion-only model already reproduces the decrease in this ratio toward higher halo masses consistent with the observation. On the other hand, for the low-mass range ($M_{\text{vir}} < 10^{12}M_\odot$), it gives a nearly constant mass ratio at each redshift, overproducing the stellar content up to two orders of magnitude. Inclusion of ejective feedback leads to a profound reduction of the stellar mass especially for low mass halos, bringing their mass ratio close to the observation. However, stellar masses for massive halos fall below the observation. The net effect of gas recycling is to lift up the final stellar mass over the entire mass range by returning some portion of the ejected gas to the disc for additional star formation. This change enlarges the discrepancy for low halo masses but remedies the deficit of stellar mass caused by ejective feedback in high-mass halos almost completely. Preventive feedback by itself affects mainly the low mass halos with $M_{\text{vir}} < 10^{12}M_\odot$ and reduces their stellar masses by ~ 1 dex with respect to the accretion-only model.

Figure 12 is similar to Figure 3 but illustrates the effect of each process on the star formation history. It is noted that the accretion-only model already creates several important features in the observed SFHs. Namely, the epoch of peak star formation is earlier and the fall of the SFR after the peak is larger for more massive galaxies especially in the high-mass range.

It is also noted that this model underproduces stars in massive systems at early times. Several possibilities can be considered for this discrepancy. The star formation law, i.e., the scaling of SFR with gas densities, adopted in the model, which is based on the local-galaxy statistics, may not apply to high- z galaxies. Or the initial mass function (IMF) may be top-heavy at early times because of low metallicity in the ISM, leading to overestimate of the observed SFR. The latter possibility can be explored in principle by incorporating a time-dependent IMF in the model and calculating the SFR indicators used in the Behroozi's analysis for direct comparison. Considering

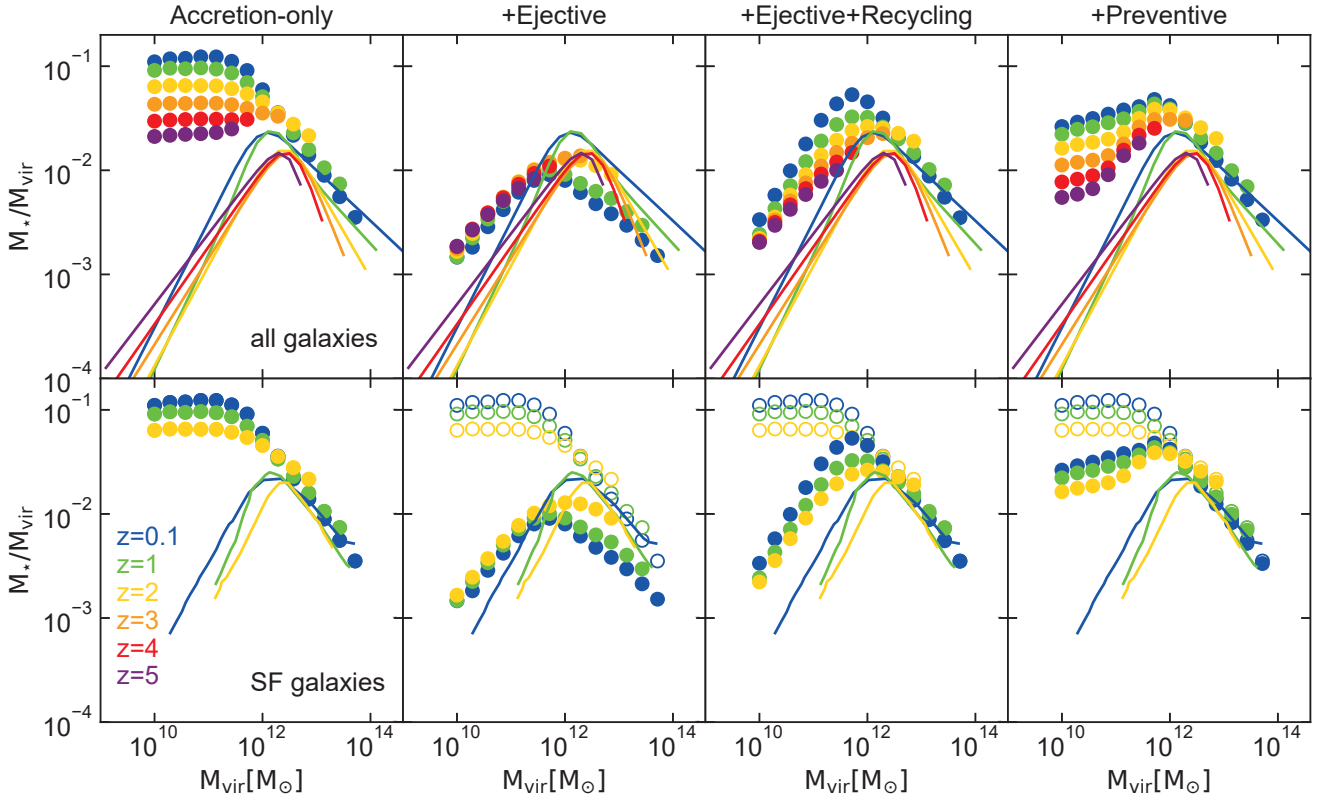


Figure 11. Same as Figure 2 but depicting the effect of feedback and recycling. Circles indicate the models with redshift colour-coded as indicated. The left-most columns show the result for the reference model in which only gas accretion in the fiducial scheme is included. Second to fourth columns show from left to right the models with ejective feedback, ejective feedback plus recycling, and preventive feedback added to the accretion-only model, respectively. The accretion-only model is replotted in the right three columns with open circles for comparison (only lower panels). The results obtained by Behroozi et al. (2019) are plotted by solid lines in top panels (all galaxies) and bottom panels (star forming galaxies) for comparison.

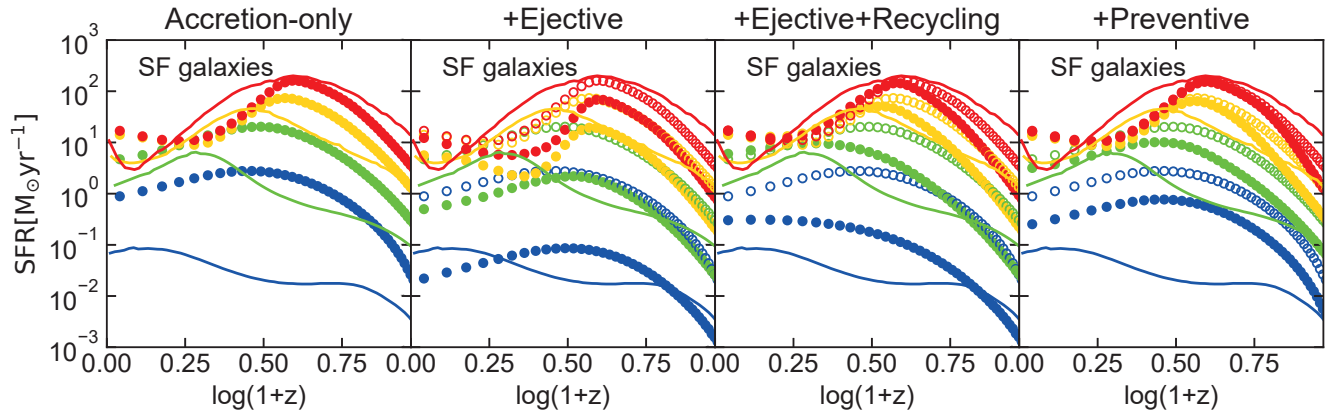


Figure 12. Same as Figure 3 but depicting the effect of feedback and recycling. Colour coding is the same as in Figure 3. Circles indicate the model while solid lines show the result by Behroozi et al. (2019). The SFHs in the accretion-only model (left-most columns) are repeatedly shown by open circles in other columns for comparison.

the crudeness of the model (e.g., the simplified treatment of gas accretion), it is not considered feasible at the moment.

All other models share the same feature as the accretion-only model for massive halos with $M_{\text{vir}} > 10^{12.5} M_{\odot}$, meaning that the cold-accretion plays a critical role and the addition of other

processes does not change the qualitative feature of the SFHs in massive halos appreciably. Ejective feedback reduces the SFR during the whole cosmological epoch with its effect getting stronger for lower halo masses. Gas recycling has a notable effect in low mass halos. It erases the peak in the SFR at $z \sim 2$ and changes

the SFH into a monotonically increasing profile. This qualitative change leads to improved match to the empirically inferred SFHs by [Behroozi et al. \(2019\)](#). This is due to the long timescale of the recycling for low mass halos implemented in the model. Namely, the recycling acts to delay star formation by taking a long time in returning the ejected gas to the disc. This change is recognized also for halos in the $10^{12}M_{\odot}$ bin (green) but is not strong enough to erase star formation peak completely. Finally, preventive feedback helps suppress over-production of stars in low mass halos but does not affect the shape of the SFR profile (Compare with the accretion-only model).

The result mentioned here is summarized more quantitatively in Figure 13. Ejective feedback and preventive feedback have negligible effect on the peak-to-minimum SFR ratio and redshift for the peak SFR, keeping the monotonically increasing trend with the halo mass. For massive halos, the peak-to-present SFR ratio are smaller than the peak-to-minimum one due to later raise of the SFR toward present. This leads to much flatter mass-dependence of this quantity. For small-mass halos, these two are equal because either the SFR monotonically decreases after the peak or the SFR monotonically increases with time. The recycling process has a remarkable effect in low mass halos ($< \sim 10^{12}M_{\odot}$), moving the peak nearer to the present epoch. This change is clearly indicated in the lower panel of Figure 13 that plots the peak redshift against the halo mass. The accretion-only model shows the peak redshift taking the minimum at intermediate mass and increasing on both sides. This feature is not destroyed by either ejective or preventive feedback. The recycling brings the model in agreement with the observation over the whole mass range by greatly reducing the peak redshift in low mass halos. Recycling also reduces the peak-to-present SFR ratio almost to unity (upper panel). The peak epoch coincides with the present time for a monotonic SFR profile.

Figure 14 plots the lookback time at which 50% of the present stellar mass is formed as a function of the present halo mass. The accretion-only model shows this critical time increasing with the halo mass but the dependence is weak. Ejective and preventive feedback preserve this property though the halos around $10^{13}M_{\odot}$ have their growth retarded considerably by ejective feedback. Except this change, we can say that the model galaxies are on the whole fairly old, reflecting the dark matter halo growth history in a Λ CDM Universe. Gas recycling causes an appreciable change by slowing the stellar mass growth in low mass halos down to ~ 5 Gyr ago, producing the downsizing behaviour. This change brings the model into a good agreement with the observational inference and also agrees with the result by the SAMs (e.g. [Henriques et al. 2013, 2015; Mitra, Davé & Finlator 2015](#)). Delay in stellar mass growth for $10^{13}M_{\odot}$ halos mentioned above is somewhat unexpected behaviour. We touch on this point later.

These results highlight the way in which the qualitatively different SFHs in high-mass and low-mass halos are brought about by the dominant processes acting on each mass domain. The transition from the cold mode to the hot mode of gas accretion makes a backbone for the SFHs in massive halos with the present mass larger than $\sim 10^{12}M_{\odot}$. In low mass halos, gas recycling plays an essential role in delaying star formation and changing the shape of SFH to a monotonically increasing profile. This is not achieved by either ejective or preventive feedback. Inability of ejective feedback in shifting SF to recent epochs and therefore making low-mass galaxies younger is also demonstrated by [Weinmann et al. \(2012\)](#). The delay seen here is due to the long recycling timescale for these halos. We take a detailed look at this point here.

Figure 15 (solid coloured lines) shows the mass and redshift

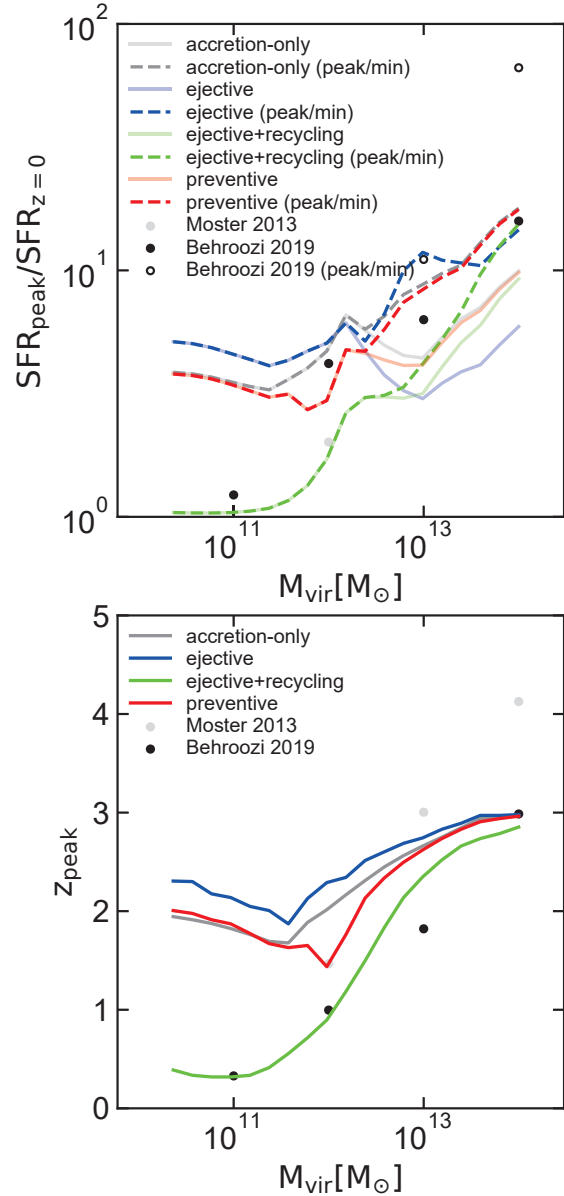


Figure 13. Upper panel: The ratio of the peak SFR and the present SFR (solid lines) or the minimum SFR (dashed lines) as a function of the present halo virial mass. Lower panel: The redshift at which the peak SFR is attained as a function of the present halo virial mass. Grey and black circles show the empirically obtained values in [Moster, Naab & White \(2013\)](#) and [Behroozi et al. \(2019\)](#), respectively.

dependence of the recycling time scale t_{rec} assumed in the present study. It is the prescription used in [Mitra, Davé & Finlator \(2015\)](#). The recycling timescale increases for lower halo masses and lower redshifts. For reference, the dashed coloured lines indicate the free-fall time at R_{vir} (upper group) and $0.25R_{\text{vir}}$ (lower group), respectively. The former is representative of the halo free-fall time. The latter radius defines roughly the inner radius of the circumgalactic region (CGR) used in the analysis of cosmological simulations (e.g. [Muratov et al. 2015](#)). The halo free-fall time depends on redshift

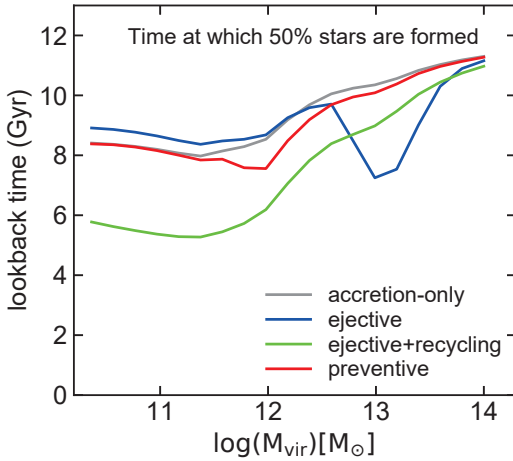


Figure 14. The lookback time at which half the present stellar mass was formed as a function of the present halo mass. Different colours indicate models in which different processes are included as indicated.

but not the halo mass due to the definition of the virial radius. The free-fall time at $0.25R_{\text{vir}}$ is not strictly constant with the mass because of the mass dependence of the halo concentration. It should be also noted that the free-fall time here is calculated from the dark matter density profile and does not include either the contribution of the baryonic component or the effect of the baryon-induced halo contraction. It therefore gives only the upper limit.

The free-fall time, t_{ff} , decreases with decreasing radius. If $t_{\text{rec}} < t_{\text{ff}}(R_{\text{vir}})$, there should be some radius r_{turn} where $t_{\text{rec}} = t_{\text{ff}}(r_{\text{turn}})$. If we assume that the ejected material reaches to the turning radius very rapidly and fall backs almost ballistically (i.e., in free-fall fashion), then r_{turn} is considered to give rough estimate for the maximum distance from the halo centre which can be reached by the ejected ISM.

It is seen that the adopted recycling time is comparable to or shorter than the halo free-fall time on the whole. Therefore, our prescription implicitly means that most of the ejected ISM cannot escape from the parent halo into the intergalactic space. We note here in passing that the mass of the ejected ISM in our energy-driven feedback is calculated under the requirement that the ejecta have the escape velocity of the dark matter halo and can therefore reach to the virial radius unless decelerated by some mechanism(s). The free-fall time at $0.25R_{\text{vir}}$ falls below the recycling time for the halo mass less than $\sim 10^{12}M_{\odot}$ for all redshift. The ejected ISM in these halos can thus reach the CGR. On the other hand, more massive galaxies have the recycling time comparable or shorter than the circumgalactic free-fall time $t_{\text{ff}}(0.25R_{\text{vir}})$. In this case, the ejected ISM must return to the disc very rapidly. Such a short recycling time physically allows the extreme case in which the feedback energy cannot push the surrounding ISM outside the disc but only puff it up. The notion of gas recycling loses its meaning in such a situation. In this study, this occurs only in relatively massive halos with $M_{\text{vir}} > 10^{12}M_{\odot}$, for which the recycling plays a subdominant role.

Cosmological simulations give useful and more direct information for comparison. It should be noted that the definition of the recycling time is not necessarily the same. For example, Christensen et al. (2016), Angl ez-Alc azar et al. (2017) and Mitchell, Schaye & Bower (2020) define t_{rec} as the time interval between ejection from the central galaxy and subsequent re-accretion on to its ISM. On the other hand, Oppenheimer et al. (2010) and Grand et al. (2019)

define t_{rec} as the interval between ejection and re-ejection/ star particle conversion, which additionally includes the time spent by the ejected gas within the ISM as gas component. Tollet et al. (2019) give only the time the ejected gas spends as cold circumgalactic gas (namely, that gas is not required to reaccrete on to the parent galaxy). This situation makes the comparison of different simulations not straightforward (see discussion in Mitchell, Schaye & Bower (2020)).

Bearing this caveat in mind, Figure 15 compares our recipe with these simulations. The cosmological simulations by Christensen et al. (2016), EAGLE, and NIHAO indicate the recycling time of the order of 1 Gyr for halo masses smaller than $\sim 10^{12}M_{\odot}$ that corresponds to $M_{\star} < 10^{10}M_{\odot}$, in rough agreement with the prescription adopted here, although the mass dependence suggested by these simulations is much weaker. The simulations by Oppenheimer et al. (2010) give systematically longer recycling times for most of the mass range whereas FIRE simulation by Angl ez-Alc azar et al. (2017) indicates shorter timescales. Our prescription lies roughly in the domain spanned by these simulations.

As discussed above, the recycling time prescription adopted in our study is not incompatible with the conceptual process that the part of the ISM launched by feedback is delivered deeply into the circumgalactic space and re-accretes to the disc after a certain time. In relation to this, cosmological simulations give direct measurements of the maximum distance the ejected gas travels before falling back to inner regions. Grand et al. (2019) report the typical maximum distance of ~ 20 kpc while Mitchell, Schaye & Bower (2020) get $> \sim 0.2R_{\text{vir}}$ for the Milky Way-sized galaxies ($M_{\text{vir}} \sim 10^{12}M_{\odot}$ at $z = 0$) for $0 < z < 2.4$. Angl ez-Alc azar et al. (2017) find the median maximum distance larger than $\sim 0.2R_{\text{vir}}$ for the halo mass above $10^{11}M_{\odot}$ but decreasing toward smaller masses with $\sim 0.1R_{\text{vir}}$ (close to the galaxy-scale) at $10^{10}M_{\odot}$ for $0 < z < 3$. However, their $10^{10}M_{\odot}$ halo (m10) has the present stellar mass of only $1.8 \times 10^6M_{\odot}$, much smaller than the lowest mass $\sim 3 \times 10^7M_{\odot}$ explored in this study. Nevertheless, gas recycling likely involves a wide range of spatial scales as suggested by these simulations. It should be also noted that the simulations by Grand et al. (2019) and Mitchell, Schaye & Bower (2020) include AGN feedback in addition to stellar feedback. AGN feedback, however, is considered to have significant impact primarily for massive halos and would not affect gas ejection in low-mass halos. To summarize, available simulation data suggest that the ejected gas typically travels well outside discs before re-accretion in low-mass halos, for which gas recycling plays an important role. Finally, we just mention that the recycling gas may have already been detected as strong C IV absorbers against background quasars (Ford et al. 2014). Its suggested extent ranges from $\sim 0.1 - 0.5R_{\text{vir}}$ increasing with the halo mass (Hasan et al. 2022), in overall agreement with the result from the above-mentioned simulations.

Figure 16 visualizes the effect of each process on the star formation rate discussed above on the $M_{\text{vir}} - z$ plane. The grey shading represents the SFR in the accretion-only model. The suppression or enhancement of this SFR by each process is shown by coloured contours as indicated. The evolution tracks of two models representative of high and low mass regimes are plotted by dashed lines. Active star formation driven by the cold-mode accretion is readily recognized above $\log M_{\text{vir}} [M_{\odot}] \sim 11.5$ at $z \gtrsim 2$ ($\log(1+z) \gtrsim 0.5$). It is noted that a new domain appears for massive halos (blue circle) in contours for ejective feedback, where the SFR is more suppressed than in the surrounding region. It is usually considered that supernova feedback has no significant effect in massive halos but this may not hold always especially in presence of active star forma-

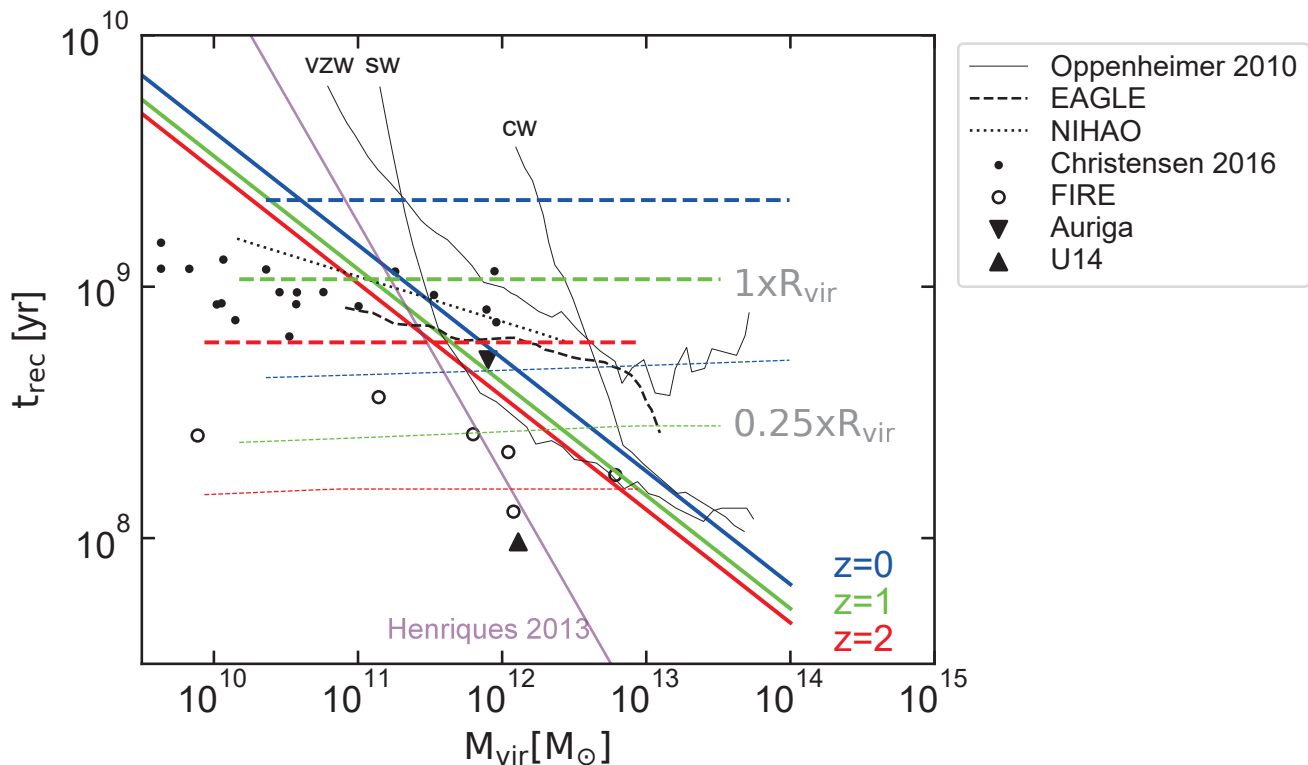


Figure 15. The recycling timescale as a function of the halo virial mass and redshift. Blue, green, and red lines indicate the dependence adopted in the present study. The purple line indicates the redshift-independent relation proportional to M_{vir}^{-1} assumed in the semi-analytic model of Henriques et al. (2013) (their equation 8). Others indicate the results of cosmological simulations for comparison. Three black lines: three simulations with different feedback recipes by Oppenheimer et al. (2010); black dashed line: EAGLE simulation by Mitchell, Schaye & Bower (2020); black dotted line: NIHAO simulation by Tollet et al. (2019); black dots: the simulation by Christensen et al. (2016); open circles: FIRE simulation by Angl ez-Alc azar et al. (2017). EAGLE, FIRE, and the simulation by Christensen et al. (2016) give the recycling time over the range $0 < z < 3$. Inverted triangle: Auriga simulation by Grand et al. (2019); triangle: the simulation by  bler et al. (2014). Two groups of coloured dashed lines indicate the free-fall time at the virial radius, R_{vir} (upper group of thick lines), and at $0.25R_{\text{vir}}$ (lower group of thin lines), respectively. They also indicate the mass range for each redshift explored in the present model.

tion activity which massive galaxies experience under cold-mode accretion.

Detailed analysis reveals that this SFR suppression is caused by the strong gas ejection associated with the preceding active star formation and leads to the small half-mass lookback time shown in Figure 14 for $M_{\text{vir}} = 10^{13}M_{\odot}$ as explained below. Figure 17 compares SFH and accretion history of the accretion-only model and the model to which only ejective feedback is added. Upper panels illustrate the relation of gas accretion rates and star formation. Grey dashed line indicates the gas accretion rate in the accretion-only model. This accretion history produces the SFH (grey solid line) that is a bit delayed from the accretion. When ejective feedback is included (blue lines), net accretion rate (blue dashed line), which is the difference between the accretion rate of the halo gas and the rate of gas ejection (blue dotted line), is reduced with respect to the accretion-only case. It decreases almost to zero after the massive ejection associated with the initial starburst, leading to steeper drop in the SFR than in the accretion-only case. Lower panel of Figure 17 shows how this feedback affects the growth of the stellar component. The magenta dashed line indicates that ejective feedback is effective in reducing the accumulation of the ISM gas (M_{g}) especially in early times because of smaller halo masses and escape velocities. What is notable here is a dip seen around 10 Gyr ago ($\log(1+z) \sim 0.4$), that is related to peak gas ejection shortly before. The effect on the SFR

(magenta solid line) is qualitatively similar to the change in M_{g} . This large dip delays the stellar mass growth by about 4 Gyr as shown by comparing grey and blue solid lines that indicates the fractional mass growth in agreement with the delay shown in Figure 14. It is interesting if this strong feedback process suggested for massive halos is observed as gas outflow in high-redshift massive galaxies.

Such a violent gas ejection also affects the gas recycling process in massive halos because the reservoir of the ejected gas increases accordingly. Figure 18 shows the relative contribution of the first-time gas accretion and the recycled accretion to the SFR in massive halos. This breakdown of instantaneous SFR was calculated as follows. The SFR in the present model is calculated from the total ISM gas mass M_{gas} as described in Appendix A3. We added an attribute to this mass that specifies the mass fractions of two components originating in the halo gas that accreted for the first time and in the recycling accretion from the ejected gas reservoir. At each timestep, we monitor the respective amounts of gas added by the halo gas accretion (i.e., first-time accretion) and by the recycling, and update the attribute correspondingly. The stars formed at each timestep inherit the attribute of the ISM gas at that timestep. Implicit assumption underlying this method is that the accreted gas with different origins is mixed completely at each time. Testing this assumption necessitates numerical simulations with much finer temporal and spacial resolution than attainable at present. We re-

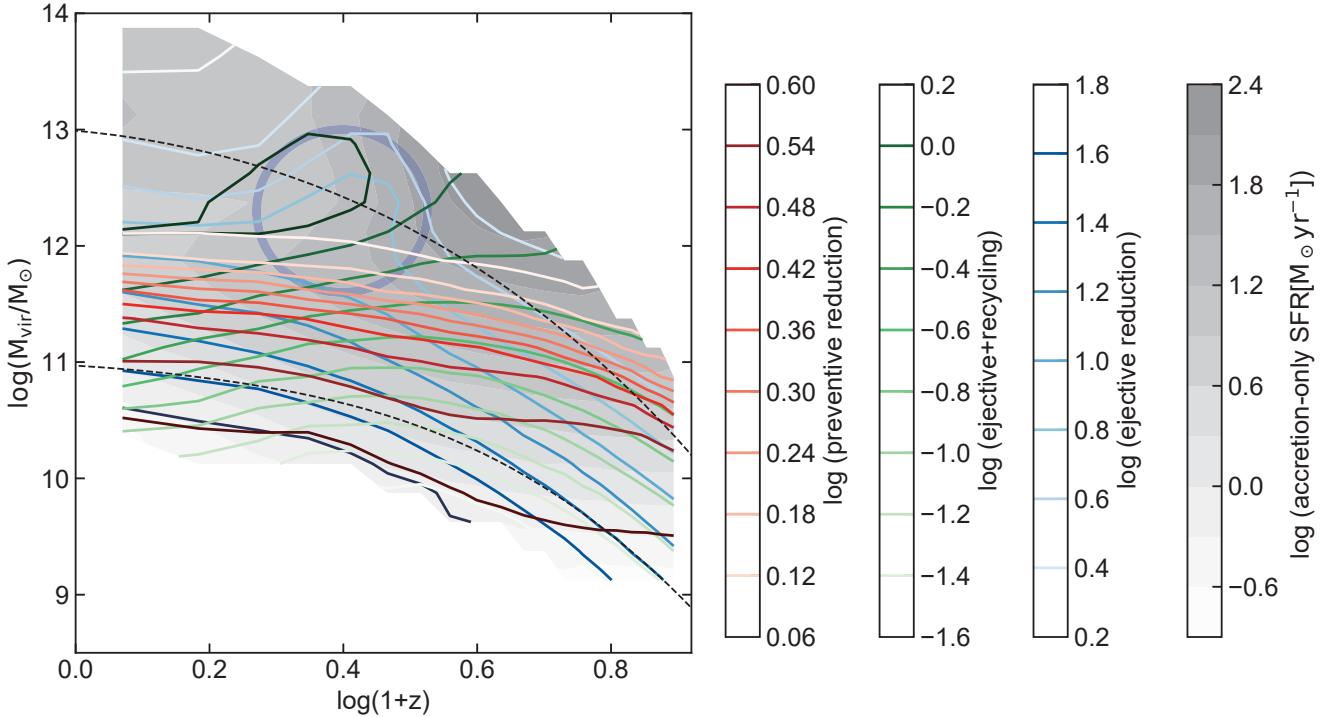


Figure 16. The effect of feedback and recycling plotted on the $M_{\text{vir}} - z$ plane. Gray shades show the star formation rate for the accretion-only model. Contours show the effect of each process on the accretion-only SFR. Ejective (blue) and preventive (red) feedback reduce the SFR especially in low-mass halos. Gas recycling partly remedies reduction of the SFR caused by ejective feedback. Combined effect of these two processes is given in the form of the SFR relative to the accretion-only SFR (green). Two dashed lines running from upper left to lower right indicate the representative pass for high-mass and low-mass halos. The blue circle indicates the domain where SFR is heavily suppressed by ejected feedback.

serve this issue as a future task and take this assumption as a caveat at the moment.

Upper panel of Figure 18 shows that the initial increase in gas accretion from the halo (grey dashed line) triggers active star formation that is delayed a bit and peaks at $\log(1+z) \sim 0.6$ (grey solid line). This starburst causes strong gas ejection with a little delay (blue dashed line). Because of short recycling time implemented, gas recycling catches up with gas ejection immediately after the peak ejection (green dashed line). Recycling-driven star formation (green solid line) follows recycling gas accretion. This chain of events brings about significant time lag between two modes of star formation. Lower panel of Figure 18 indicates the fractions of two star formation modes. Initial short period is dominated by the first-time gas accretion from the halo because there is not enough time for gas recycling to follow the gas ejection. Just after the peak SFR_{acc} , gas recycling starts to become dominant route due to time lag. Although the contribution of recycling accretion diminishes with time, it remains a major source for star formation in halos with this mass range. Because the recycling rate follows the ejection rate almost completely except initial epoch where halo and galaxy masses are small, the recycling of the ejected ISM returns most of the ejected gas in massive halos and nearly recovers the SFR in the accretion-only case as shown in Figures 11 and 15. Recovery ability of this process diminishes toward lower halo masses.

6 DISCUSSION

The present model adopting the fiducial scheme of gas accretion reproduces reasonably well several key features in the observed SFHs for a range of galaxy mass. There, however, remain issues to be clarified before we reach a more consistent picture for galactic star formation. Although the reproduction of the quantitative detail is not the purpose of this study, we here discuss several topics not touched upon in previous sections, hoping to get some hint for further study toward more comprehensive and quantitative understanding.

6.1 Degeneracy of ejective and preventive feedback

The importance of preventive feedback was suggested by the results discussed above. We introduced this process by reducing the gas accretion rate to the disc. Ejective feedback also helps suppress star formation by removing the interstellar gas. These two processes operate effectively in similar domains in the $M_{\text{vir}} - z$ plane (Figure 16), suggesting a possibility that these processes are degenerate. Namely, a question arises whether ejective feedback with properly adjusted parameters can serve as a substitute for the required preventive feedback.

To explore this possibility, we first turned off preventive feedback and increased the efficiency of ejective feedback up to unity (i.e., all the energy liberated by supernovae is used in ejecting the ISM). For any choice in this range ($0.2 < \varepsilon_{\text{FB}} < 1$), the replacement by ejective feedback exacerbates the poor fit to the observed stellar-to-halo mass ratio. Matching the ratio for low mass halos inevitably leads to unacceptable underproduction of the stellar content

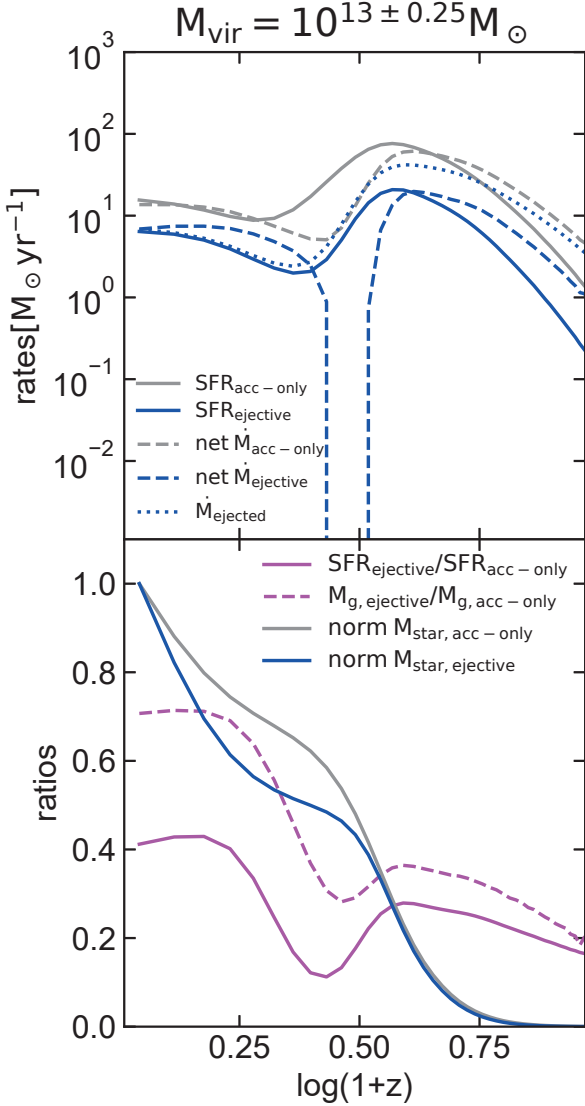


Figure 17. The effects of ejective feedback on the evolution of the ISM and the stellar component in halos of $M_{\text{vir}} = 10^{13} M_{\odot}$ in the fiducial accretion scheme. Upper panel: Rates of gas accretion, ejection and star formation. Grey and blue lines show the result for the accretion-only model and the model to which ejective feedback is added (corresponding to those two models plotted in Figure 12). $\text{net } \dot{M}_{\text{ejective}}$ is the accretion-only accretion rate (grey dashed line) minus the gas ejection rate (blue dotted line). Lower panel: Relative reduction of the gas mass (M_{g}) and SFR (magenta lines) caused by ejective feedback. Grey and blue lines indicate the fractional stellar mass growth in the two models.

for high mass halos. This may be due to the steep V_{vir}^{-2} dependence of the energy-driven feedback adopted here (V_{vir} is the virial velocity of the halo). We next tried the momentum feedback with the V_{vir}^{-1} dependence. This choice did not give a satisfactory agreement either. This result means that raising the ejection efficiency above the fiducial value is not a promising replacement for preventive feedback.

This in turn casts a doubt that the efficiency of 20% adopted for the fiducial ejective feedback may already be too large. In order to check this point, we examined the mass loading factor (i.e., the ratio of the mass ejection rate and the SFR, hereafter MLF) in the

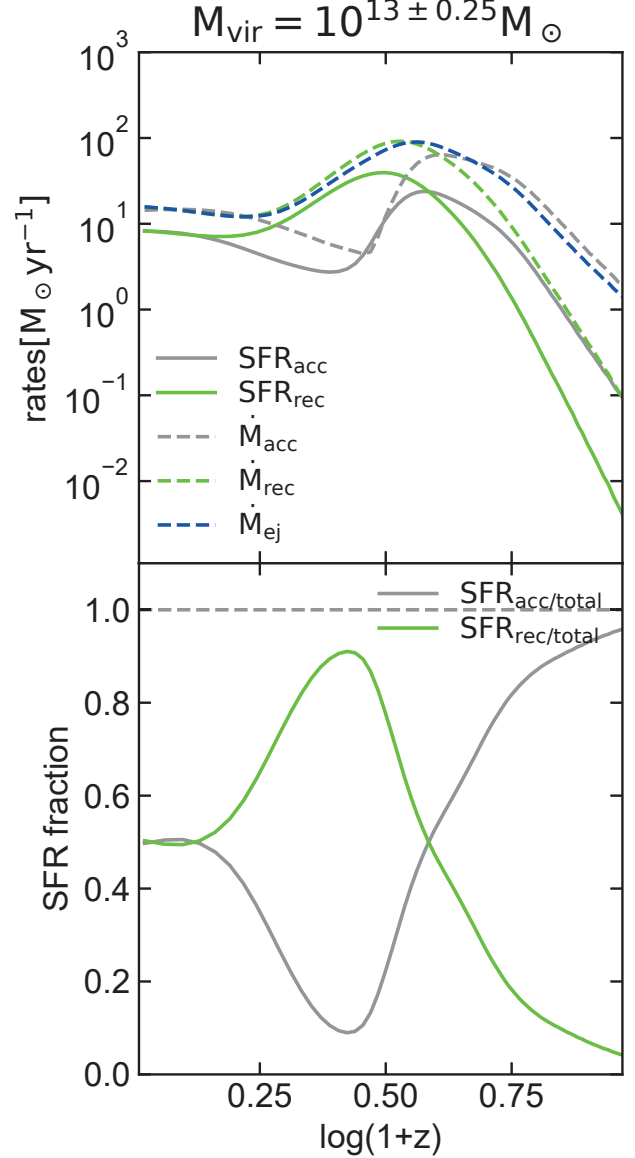


Figure 18. Relative contribution of first-time gas accretion and recycling gas accretion in star formation for the full model with $M_{\text{vir}} = 10^{13} M_{\odot}$ in the fiducial scheme. Upper panel: Breakdown of the SFR into two components with two different accretion routes. Rates of first-time accretion, ejection and recycling accretion are plotted with dashed lines. Lower panel: Fraction of each SFR component with respect to the total SFR.

present model. Figure 19 compares our fiducial-scheme model with available observations and other theoretical models. The MLFs for the efficiency $\varepsilon_{\text{FB}} = 0.2$ roughly border the upper envelope for the observational data. In the low mass domain where feedback has dominant effect, the semi-analytic model by Lagos, Lacey & Baugh (2013) and Illustris simulation by Vogelsberger et al. (2013) give higher MLFs than our model while other cosmological simulations and the steady state models by Hopkins, Quataert & Murray (2012) show lower values.

Considering this result, we lowered the efficiency to $\varepsilon_{\text{FB}} = 0.05$. This brings the model in better agreement with the observation and the theoretical results. For this value, massive halos suffer from

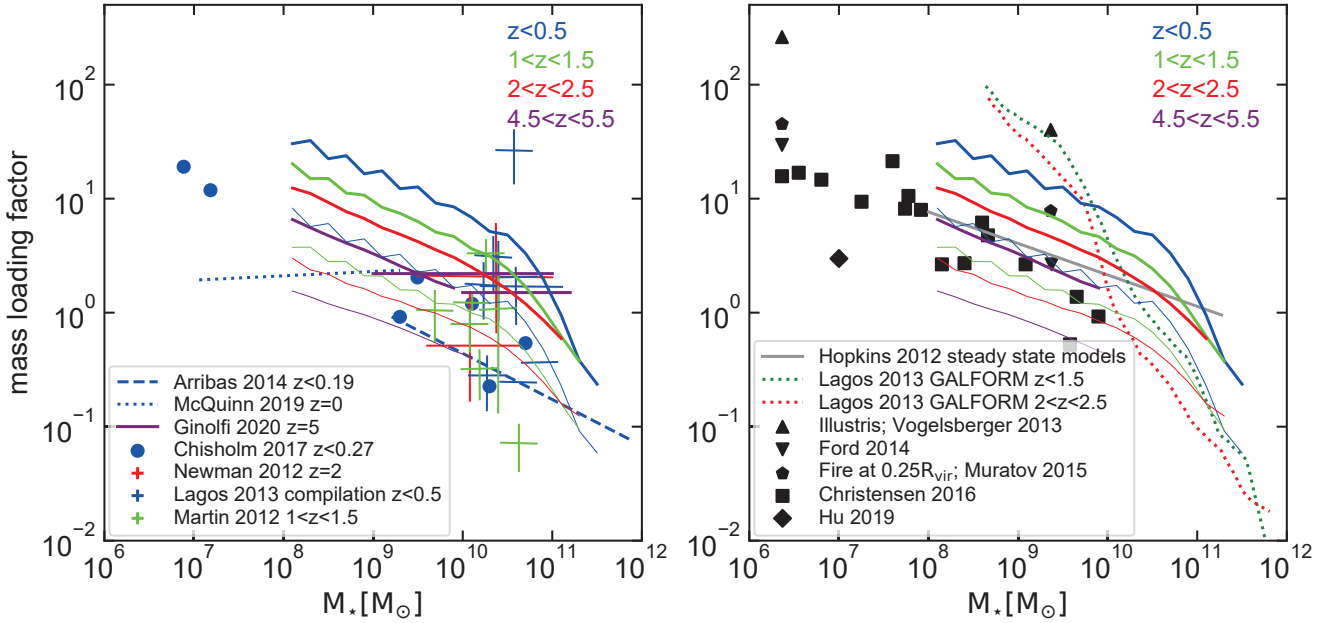


Figure 19. Mass loading factors obtained in the present model compared with the observation (left) and previous theoretical studies (right). Redshift is colour-coded as indicated. Thick and thin solid lines indicate the models in the fiducial scheme with the feedback efficiency of 0.2 and 0.05, respectively. Left panel: Observational results are shown by Arribas et al. (2014), Chisholm et al. (2017), Ginolfi et al. (2020), Marasco, Fraternali & Binney (2012) and McQuinn, van Zee & Skillman (2019) (The observation by Ginolfi et al. (2020) is two horizontal purple lines). Blue crosses and short horizontal segments represent the results by various authors for nearby galaxies (see Fig. 14 of Lagos, Lacey & Baugh (2013) for details). Right panel: The numerical simulation for steady state models by Hopkins, Quataert & Murray (2012) is indicated by the grey solid line because no redshift is specified. The semi-analytic model (GALFORM) by Lagos, Lacey & Baugh (2013) for $z < 1.5$ and $2 < z < 2.5$ is indicated by green and red dotted lines, respectively. Black symbols indicate the results by cosmological simulations for $z = 0$ from Vogelsberger et al. (2013), Ford et al. (2014), Muratov et al. (2015), Christensen et al. (2016) and Hu (2019).

negligible effect of ejective feedback. In this case, however, we need much stronger action of preventive feedback that reduces the gas accretion rate to $\sim 5\%$ instead of the adopted 30% in order to match the stellar mass in low-mass galaxies. This leads to the contribution in the stellar mass reduction being comparable between two types of feedback while the contribution of ejective feedback is about twice that by preventive feedback in the $\varepsilon_{\text{FB}} = 0.2$ case. It is not clear if such a strong preventive feedback is possible. Because the observationally derived MLFs likely give only lower limits (but also see the discussion by McQuinn, van Zee & Skillman (2019)), the ejective efficiency of 20% may not necessarily be unrealistic. Incidentally, Dutton & van den Bosch (2009) found that $\sim 25\%$ of the supernova energy is required to reproduce the scaling relations of disc galaxies although this conclusion was derived for the shock-heating picture. In any case, it seems robust that we need a significant contribution from preventive feedback to explain the stellar mass budget over the whole mass range.

6.2 Comparison of the adopted preventive feedback to previous works

The importance of prevented feedback has been stressed also from the chemical point of view (e.g. Mitra, Davé & Finlator 2015; Christensen et al. 2016). It is well known that there is a tension between low efficiency of making stars and retaining enough metal in low-mass galaxies. The model that relies solely on ejective feedback in reducing stellar masses produces a too steep mass-metallicity relation compared with the observation (e.g. Torrey et al. 2014;

Somerville, Popping & Trager 2015). Preventive feedback can reduce the stellar mass in low mass galaxies with their metallicity nearly untouched (e.g. Torrey et al. 2014). For example, the cosmological simulation by Christensen et al. (2016) that includes preventive feedback produces the mass-metallicity relation at $z = 0$ with the slope and normalization agreeing with the observation.

We have seen above that preventive feedback is required also to reproduce the stellar-to-halo mass ratio for low mass galaxies. Nevertheless, preventive feedback is here introduced in an ad-hoc manner tuned for better reproduction of the observational data. It is important to check the plausibility of the introduced prescription to describe this process. Because there is no strong constraint from the observation at the moment, we compare the outcome of our prescription to the cosmological simulations addressing this process. The red line in the left panel of Figure 20 indicates the critical halo mass for preventive feedback adopted in this study. Two asterisks indicate the halo mass below which the inclusion of stellar feedback reduces the gas accretion rate on to halos in the simulation by van de Voort et al. (2011). Simulations by Correa et al. (2018) and Wright et al. (2020) give similar results. Two triangles denote the mass below which the prevented gas starts to dominate the total baryon mass budget in EAGLE simulation performed by Mitchell & Schaye (2022). Our prescription agrees with these cosmological simulations at least up to $z \sim 2$. The FIRE-2 cosmological simulation by Hopkins et al. (2018) and the SAM by Pandya et al. (2020) also suggest the critical mass for preventive feedback caused by supernovae that decreases with redshift. Their critical masses lie in the range $10^{11} - 10^{12} M_\odot$ in agreement with our prescription

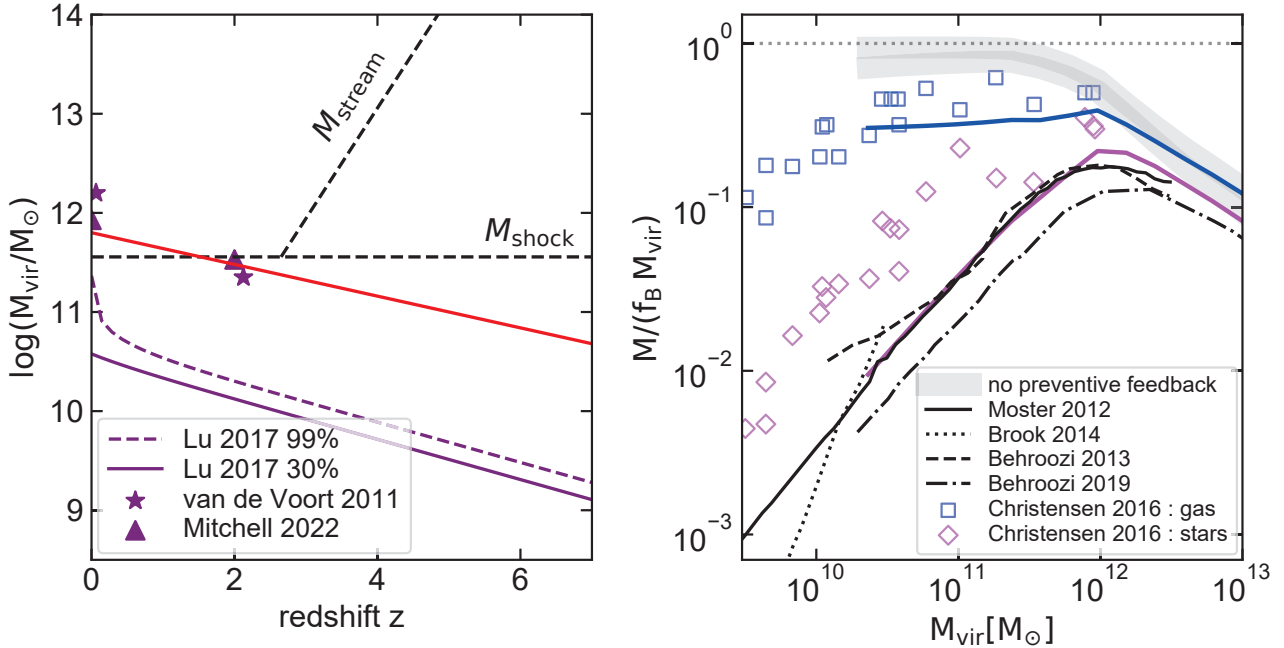


Figure 20. Preventive feedback in this study compared with other works. Left: The critical halo mass below which the gas accretion is prevented is indicated by the red line. Purple lines indicate the halo mass at which 99% and 30% of the gas is accreted in the prescription used by Lu et al. (2017). Asterisks and triangles indicate the mass below which the gas accretion is suppressed in the cosmological simulations by van de Voort et al. (2011) and Mitchell & Schaye (2022), respectively. Right: Masses of stars and gas present in the disc at $z = 0$ as a function of the halo virial mass. Masses are normalized by the cosmic baryon fraction times the virial mass. Blue and magenta solid lines indicate the gaseous and stellar masses for the full model in the fiducial scheme while gray broad lines indicate the model in which no preventive feedback is included. Squares indicate the gas accreted to the disc in the simulation by Christensen et al. (2016) for direct comparison with the present model in which the prevention is modelled as the reduction of accretion on to discs (not to halos). Diamonds indicate the stellar mass in the disc from the same simulation. Black lines denote the results obtained by the abundance matching technique by the indicated authors.

and other cosmological simulations. Analytical prescription considered in Davé, Finlator & Oppenheimer (2012) adopts systematically lower efficiency than our choice over the redshift range $0 < z < 2$ and applies to lower halo masses. Nevertheless, their recipe dictates stronger feedback for higher redshifts and less massive halos, which is qualitatively similar to our recipe.

Right panel of Figure 20 shows that the decrease in the gas accretion due to preventive feedback is around 30 ~ 40% for $M_{\text{vir}} < 10^{12} M_{\odot}$ in our fiducial-scheme model. This diminishment is comparable to the one obtained in the cosmological simulation by Christensen et al. (2016). For the stellar mass, our model gives much smaller values but in agreement with the empirical estimates for the stellar-to-halo mass ratios. This fact may lend some support to the recipe adopted in the present work.

Lu et al. (2017) parametrized the strength of preventive feedback as a function of halo mass and redshift by fitting their semi-analytic model to the stellar mass function and the mass-metallicity relation of the satellite galaxies of Milky Way. Dashed and solid purple lines in the left panel indicate the halo mass for which the accretion to the halo is reduced to respectively 99% and 30% with respect to $f_{\text{bar}} \dot{M}_{\text{vir}}$. These masses are much lower than our recipe and other studies mentioned above, rather in agreement with the boundary for UV background suppression given by Gnedin (2000) and Okamoto, Gao & Theuns (2008) (see Figure 1). Their model thus seems to imply that the background radiation field is sufficient in preventing gas accretion in the Milky Way system. By contrast, other studies suggest a close link between ejective and preventive

feedback. For example, Oppenheimer et al. (2010), based on the numerical simulations, argue that the suppression of gas accretion by supernova wind energy and momentum has a strong effect for low mass galaxies. van de Voort et al. (2011) and Muratov et al. (2015) also appear to support this picture.

The suggested dominance of preventive feedback for low mass halos may demand significant revision of the cold accretion picture for the low-mass regime. Possible interactions between the outgoing gas ejecta and the inflowing cold gas may change the physical state of the halo gas drastically. In other words, preventive feedback by definition invalidates the assumption of the universal baryon fraction in parent halos and/or the gas accretion rate (on to discs) calculated from either the free-fall time or the radiative cooling time. Nevertheless, we could gauge the required suppression of gas accretion on to galaxies relative to the accretion rate calculated from the universal baryon fraction and appropriate inflow timescales (also see Appendix, section A6).

6.3 Missing processes

The present study demonstrates the ability of simple isolated models in reproducing the observed diversity in galactic star formation history. This success is attained by assuming the cold accretion regime of halo gas acquisition and cooperation of ejective feedback, preventive feedback and gas recycling. This study reveals at the same time several shortcomings of these idealized models. The most notable disagreement with the observational data is that the

models underpredict SFR at high redshifts. At low redshifts, massive galaxies show higher SFRs than observed. Here we discuss several processes which are neglected in our models but may resolve or alleviate these problems. Specifically, we touch on here AGN feedback, galaxy mergers and wind transfer.

The most promising process to reduce high SFR in massive galaxies in recent epochs is feedback from AGNs. It has been considered to be one of important processes that potentially affect the galaxy evolution and has been taken into account in many theoretical studies (e.g. Sijacki et al. 2007; Vogelsberger et al. 2013; Weinberger et al. 2018). These studies (both the SAMs and cosmological simulations) succeeded in explaining the quenching of massive galaxies by introducing AGN feedback (e.g. Kauffmann & Haehnelt 2000; Croton et al. 2006; de Lucia et al. 2010; Lu et al. 2014). Quenching mechanisms can act in various forms. For example, radio mode feedback can act as preventive feedback (e.g. Kereš et al. 2009; Zinger et al. 2020) and may lead to ‘halo quenching’ as discussed by Lu et al. (2014). The accumulation of AGNs on way from the blue cloud to the red sequence for late type galaxies (e.g. Schawinski et al. 2010; Powell et al. 2017) may suggest AGN-quenching for star forming galaxies from the observational viewpoint. McPartland et al. (2019) report that the inclusion of AGNs (LINERs and Seyfert 2 galaxies) into observational analysis leads to the turn-over of the MS at high masses. On the other hand, de Lucia et al. (2010), using a semi-analytic model, argue that the necessity of AGN feedback is changed by various assumptions adopted for gas cooling. Recent cosmological simulations (e.g. Correa et al. 2018; Nelson et al. 2019; Wright et al. 2020) give more quantitative results for the effect of AGN feedback on gas accretion rates. For example, Wright et al. (2020) indicate that stellar feedback has much stronger preventative effect than AGN feedback (factor ~ 4 versus $20 \sim 30\%$). They infer that this difference is due partially to the former acting preferentially in low mass halos that have shallow gravitational potentials while the latter operates in massive halos having deep potential wells. Our result also suggests that preventive feedback is more important in low mass halos in line with these simulation result (e.g., Figure 16). Probably, one of the most relevant results to the current issue is provided by the EAGLE simulation (Katsianis et al. 2017) which shows that AGN feedback at low redshifts improves the agreement of the simulation with the observed evolution of the cosmic SFR density (CSFRD) (see their Figure 10). Although CSFRD is the integrated quantity over all galaxy populations, this result hints at important role of AGN feedback in quenching massive galaxies in recent epochs. This result suggests that inclusion of AGN feedback could help cure unrealistic upturn in SFR in low-redshift massive galaxies seen in the present fiducial scheme.

Regrettably, most observational works conducted to date (e.g. Schawinski et al. 2010; McQuinn, van Zee & Skillman 2019) give only circumstantial evidence for AGN quenching. More direct information could be provided by measuring the mass loading factor for AGN-driven outflows. For example, Qiu et al. (2021) calculated the ratio of outflow rate and black hole accretion rate for massive elliptical galaxies. If some scaling relation between this ratio and the BH accretion rate or BH mass is established by extending such analysis to larger samples including late-type galaxies, it could be combined with the BH growth model to provide better theoretical insight into the importance of AGN feedback for different galaxy masses and cosmological epochs.

On the other hand, overly inactive star formation in model galaxies at high redshift could be alleviated by galaxy mergers which are expected to be frequent at early cosmological epochs. Along with AGN feedback, galaxy mergers have also been considered as

an important process affecting mainly massive galaxies. They can provide a promising route for morphological transformation and star formation quenching, both processes possibly leading to the formation of early-type (elliptical) galaxies. One concern with this scenario is that mergers may not quench star formation completely. For example, the simulation by Springel, Di Matteo & Hernquist (2005) indicates that the aid from AGN feedback is necessary to expell the residual ISM completely outside merging galaxies. Despite this caveat, it seems evident that galaxy mergers (especially major ones) have non-negligible effects on the evolution of galaxy populations. Including mergers is difficult in our modelling by construction. Therefore, the present model should be, in the strict sense, regarded as mainly describing evolution of disc-dominated galaxies that have probably suffered little from the effects of major galaxy mergers in their lives. Although the merger-driven starbursts in disc galaxies are thus not handled in our current model, it seems reasonable to expect that frequent mergers in early times would enhance star formation activity by perturbing young gas-rich galactic discs.

Recent cosmological simulations (e.g. Angl ez-Alc azar et al. 2017; Grand et al. 2019; Mitchell, Schaye & Bower 2020) point out the importance of intergalactic transfer of material such as ‘wind transfer’ in addition to mergers of galaxies themselves. These simulations suggest comparable contribution of this process to other processes such as gas recycling (fountain flow) and fresh gas accretion. Our model is unable to predict how these extragalactic ingredients affect galaxy evolution. What is naturally expected is that the idealized concept of hot and cold modes of gas accretion depicted in Figure 1 may be significantly modified (in addition to possible modification posed by preventive feedback mentioned in section 6.2). Currently, the definition of these newly introduced processes itself varies among different authors and mutual comparison of simulation results is not straightforward. It is challenging but worthwhile to forge various processes occurring on halo scales into a unified picture as the next target.

7 CONCLUSIONS

We constructed a simple model for the evolution of galactic stellar contents in order to investigate how the star formation history is affected by gas accretion process from host halos. We consider three different schemes of gas accretion. The shock-heating scheme assumes that the gas gathered by halos experiences heating by shock waves to the virial temperature and subsequent radiative cooling induces gas accretion. According to the stability analysis of shock waves, low mass halos experience rapid free-fall accretion of unheated gas due to instability irrespective of redshift. The flat scheme takes this picture. Finally, the fiducial scheme assumes efficient accretion driven by filamentary streaming of cold gas through the shock-heated hot gas in massive halos at high redshift, in addition to the cold-mode accretion induced by shock instability in the low mass domain. In addition to gas accretion, the model includes two types of feedback; ejective feedback by supernova energy and preventive feedback that hinders some portion of the halo gas from accreting on to galactic discs. Re-accretion (recycling) of the interstellar medium ejected by supernovae is also taken into account.

The fiducial scheme reproduces several key features of the observational results regarding the star formation activity in massive galaxies. The early occurrence of the star formation peak and the strong diminishment of the star formation rate after that are reproduced at least qualitatively. Moreover, the slope of the high-mass domain in the SFR- M_\star relation (MS) decreases with time

in agreement with observations. On the other hand, the flat and shock-heating schemes predict similar SFHs in massive halos that qualitatively contradict observations. Namely, SFRs increase with time nearly monotonically and the high-mass end of MS shows steeper slopes toward recent epochs. The transition from the cold to hot modes of halo gas accretion, which roughly marks peak star formation activity, is an important piece in shaping the star formation history in massive halos. Retardation of this transition in the fiducial scheme caused by inflow of cold gas streams in high-mass high-redshift domain leads to a larger gap in accretion timescale and therefore a more drastic drop in accretion rate and SFR.

In contrast to massive halos, low-mass halos evolve under rapid gas accretion in all accretion schemes. In the presence of only accretion, they experience active star formation in early epochs reflecting growing history of their parent halos, leading to too massive stellar components and old ages at present time. Comparable contribution of supernova feedback and preventive feedback seems to be required to reduce their stellar masses to the observed level. Recycling of the ejected interstellar medium with the timescale of ~ 1 Gyr plays an essential role in producing monotonically increasing SFR and thus making these galaxies young enough to match the observation. In the fiducial scheme, this change in SFHs of low mass halos and the early strong quenching in massive halos lead to the downsizing galaxy formation as observed.

ACKNOWLEDGEMENTS

We thank Camilla Pacifici, Gergő Popping, Kate Whitaker for providing their data. Data compilations for other studies used in this paper were made by using the online `WEBPLOTDIGITIZER` code.¹

DATA AVAILABILITY

The data underlying this article will be shared on reasonable request to the corresponding author.

REFERENCES

- Abramson L.E. et al., 2014, *ApJ*, 785, L36
 Aguerri J. A. L., Mendez-Abreu J., Corsini, E. M., 2009, *A&A*, 495, 491
 Angl ez-Alc azar D. et al., 2017, *MNRAS*, 470, 4698
 Arribas S. et al., 2014, *A&A*, 568, A14
 Barazza F. D., Jooe S., Marinova I., 2008, *ApJ*, 675, 1194
 Behroozi P. et al., 2019, *MNRAS*, 488, 3143
 Behroozi P.S., Wechsler R.H., Conroy C., 2013, *ApJ*, 770, 57
 Bigiel F. et al., 2008, *AJ*, 136, 2846
 Birnboim Y., Dekel A., 2003, *MNRAS*, 345, 349
 Birnboim Y., Dekel A., Neistein E., 2007, *MNRAS*, 380, 339
 Blitz L., Rosolowsky E., 2006, *ApJ*, 650, 933
 Bluck A.F.L. et al., 2014, *MNRAS*, 441, 599
 Blumenthal G.R. et al., 1984, *Nature*, 311, 517
 Boselli A. et al., 2014, *A&A*, 564, A66
 Bothwell M. S., Kennicutt R. C., Lee J. C., 2009, *MNRAS*, 400, 154
 Bothwell M. S. et al., 2014, *MNRAS*, 445, 2599
 Bouch e N. et al., 2010, *ApJ*, 718, 1001
 Breda I., Papaderos P., 2018, *A&A*, 614, 48
 Breda I. et al., 2020, *A&A*, 635, 177
 Brennan R. et al., 2015, *MNRAS*, 451, 2933
 Brennan R. et al., 2017, *MNRAS*, 465, 619
 Brook, C. B., Stinson, G., Gibson, B. K., et al. 2012, *MNRAS*, 419, 771
 Brooks A.M. et al., 2007, *ApJ*, 655, L17
 Bullock J.S. et al., 2001, *MNRAS*, 321, 559
 Bullock J.S., Boylan-Kolchin M., 2017, *ARAA*, 55, 343
 Cano-D az M. et al., 2019, *MNRAS*, 488, 3929
 Catinella B. et al., 2010, *MNRAS*, 403, 683
 Cattaneo A. et al., 2006, *MNRAS*, 370, 1651
 Cattaneo A., Koutsouridou I., Tollet E. et al., 2020, *MNRAS*, 497, 279
 Ceverino D., Klypin A., 2009, *ApJ*, 695, 292
 Chabrier G., 2003, *PASP*, 115, 763
 Cheung E. et al., 2013, *ApJ*, 779, 162
 Chisholm J. et al., 2015, *ApJ*, 811, 149
 Chisholm J. et al., 2017, *MNRAS*, 469, 4831
 Christensen C.R. et al., 2016, *ApJ*, 824, 57
 Coil A.L. et al., 2011, *ApJ*, 741, 8
 Cole S. et al., 1994, *MNRAS*, 271, 781
 Cook R.H.W. et al., 2020, *MNRAS*, 493, 5596
 Corcho-Caballero P., Ascasibar Y., L opez-S anchez A.R., 2020, *MNRAS*, 499, 573
 Correa C.A. et al., 2018, *MNRAS*, 478, 225
 Croton D. J. et al., 2006, *MNRAS*, 365, 11
 Croton D. J. et al., 2016, *ApJS*, 222, 22
 Dav e R., Finlator K., Oppenheimer B.D., 2012, *MNRAS*, 421, 98
 Dav e R. et al., 2013, *MNRAS*, 434, 2645
 Dekel A., Birnboim Y., 2006, *MNRAS*, 368, 2
 Dekel A., Silk J., 1986, *ApJ*, 303, 39
 Dekel A. et al., 2009, *Nature*, 457, 451
 de Lucia G., Blaizot J., 2007, *MNRAS*, 375, 2
 de Lucia G. et al., 2010, *MNRAS*, 406, 1533
 Dessauges-Zavadsky M. et al., 2020, *A&A*, 643, 5
 Donnari M. et al., 2019, *MNRAS*, 485, 4817
 Dutton A.A., van den Bosch, F.C., 2009, *MNRAS*, 396, 141
 Dutton A.A., van den Bosch F.C., Dekel A., 2010, *MNRAS*, 405, 1690
 Efstathiou E., 1992, *MNRAS*, 256, 43P
 Elbaz D. et al., 2007, *A&A*, 468, 33
 Elmegreen, B.G., 1993, *ApJ*, 411, 170
 Erb D.K. et al., 2006, *ApJ*, 646, 107
 Erwin P., 2018, *MNRAS*, 474, 5372
 Fabian A.C., 2012, *ARA&A*, 50, 455
 Fardal M. A. et al., 2001, *ApJ*, 562, 605
 Feldmann R., 2020, *Communications Phys.*, 3, 226
 Ford, A. B., Dave, R., Oppenheimer, B. D., et al. 2014, *MNRAS*, 444, 1260
 Fraser-McKelvie A., Merrifield M., Arag on-Salamanca A., 2019, *MNRAS*, 489, 5030
 Fraternali F., Pezzulli G., Proceedings of the International Astronomical Union , Volume 14 , Symposium A30: Astronomy in Focus XXX , August 2018 , pp. 228 - 232
 Fumagalli M. et al., 2011, *MNRAS*, 418, 1796
 Furlong M. et al., 2015, *MNRAS*, 450, 4486
 Gao Y., Solomon P.M., 2004, *ApJ*, 606, 271
 Genel S. et al., 2014, *MNRAS*, 445, 175
 Genzel R. et al., 2010, *MNRAS*, 407, 2091
 Ginolfi M. et al., 2020, *A&A*, 633, 90
 Giovanelli R., Haynes M.P., Kent B.R., et al., 2005, *AJ*, 130, 2598
 Gnedin N.Y., 2000, *ApJ*, 542, 535
 Gnedin N.Y., Kravtsov A.V., 2011, *ApJ*, 728, 88
 Grand, R.J.J. et al. 2018, *MNRAS*, 474, 3629
 Grand, R.J.J., van de Voort, F., Zjupa, J., et al. 2019, *MNRAS*, 490, 4786
 Grogin N.A. et al., 2011, *ApJS*, 197, 35
 Guo Q. et al., 2011, *MNRAS*, 413, 101
 Guo Q. et al., 2016, *MNRAS*, 461, 3457
 Hasan F. et al., 2022, *ApJ*, 924, 12
 Helfer T. T., Thornley M. D., Regan M.W., Wong T., Sheth K., Vogel S. N., Blitz L., Bock D., 2003, *ApJS*, 145, 259
 Henriques B.M.B. et al., 2013, *MNRAS*, 431, 3373
 Henriques B.M.B. et al., 2015, *MNRAS*, 451, 2663
 Hoeft M. et al., 2006, *MNRAS*, 371, 401
 Hopkins P.F., Quataert E., Murray N., 2012, *MNRAS*, 421, 3522
 Hopkins P.F. et al., 2014, *MNRAS*, 445, 581

¹ <https://automeris.io/WebPlotDigitizer/>

- Hopkins P.F. et al., 2018, MNRAS, 480, 800
 Hu, C.-Y. 2019, MNRAS, 483, 3363
 Ji Z. et al., 2018, ApJ, 862, 135
 Johnston R. et al., 2015, MNRAS, 453, 2540
 Katsianis A. et al., 2017, MNRAS, 472, 919
 Kauffmann G., Haehnelt M., 2000, MNRAS, 311, 576
 Kauffmann G., White S.D.M., Guiderdoni B., 1993, MNRAS, 264, 201
 Kennicutt R.C.Jr., 2012, ARAA, 50, 531
 Kereš D. et al., 2005, MNRAS, 363, 2
 Kereš D. et al., 2009, MNRAS, 396, 2332
 Khusanova Y. et al., 2021, A&A, 649, 152
 Klypin A.A., Trujillo-Gomez S., Primack J., 2011, ApJ, 740, 102
 Koekemoer A.M., et al., 2011, ApJS, 197, 36
 Kurczynski P. et al., 2016, ApJ, 820, L1
 Lacey C.G. et al., 1993, ApJ, 402, 15
 Lacey C.G. et al., 2016, MNRAS, 462, 3854
 Lagos C.D.P., Lacey C.G., Baugh C.M., 2013, MNRAS, 436, 1787
 Lagos C.D.P. et al., 2014, MNRAS, 440, 920
 Lapi A. et al., 2020, ApJ, 897, 81
 Leroy A. K. et al., 2008, AJ, 136, 2782
 Liu D. et al., 2019, ApJ, 887, 235
 Lu Y. et al., 2014, ApJ, 795, 123
 Lu Z. et al., 2017, ApJ, 846, 66
 Macciò A.V., Dutton A.A., van den Bosch, F.C., 2008, MNRAS, 391, 1940
 Mac Low M.-M., Ferrara A., 1999, ApJ, 513, 142
 Mandelbaum R., Seljak U., Kauffmann G., Hirata C.M., Brinkmann J., 2006, MNRAS, 368, 715
 Marasco, A., Fraternali, F., Binney, J.J. 2012, MNRAS, 419, 1107
 Martin, D. C., et al. 2005, ApJ, 619, L1
 Martin D. C. et al., 2016, ApJ, 824, L5
 McGaugh S. S., 2012, AJ, 143, 40
 McPartland C. et al., 2019, MNRAS, 482, L129
 McQuinn K.B.W., van Zee L., Skillman E.D., 2019, ApJ, 886, 74
 Medling A.M. et al., 2018, MNRAS, 475, 5194
 Mitchell P.D. et al., 2014, MNRAS, 444, 2637
 Mitchell P.D. et al., 2018, MNRAS, 474, 492
 Mitchell P.D., Schaye J., Bower R.G., 2020, MNRAS, 497, 4495
 Mitchell P.D., Schaye J., 2022, MNRAS, 511, 2600
 Mitra S., Davé R., Finlator K., 2015, MNRAS, 452, 1184
 Monaco P., Fontanot F., Taffoni G., 2007, MNRAS, 375, 1189
 More S., van den Bosch F.C., Cacciato M., Skibba R., Mo H.J., Yang X., 2011, MNRAS, 410, 210
 Moster B.P., Naab T., White S.D.M., 2013, MNRAS, 428, 3121
 Moster B.P., Naab T., White S.D.M., 2018, MNRAS, 477, 1822
 Moster B.P., et al., 2021, MNRAS, 507, 2115
 Muratov, A. L., Kereš, D., Faucher-Giguere, C.-A., et al. 2015, MNRAS, 454, 2691
 Murray N., Quataert E., Thompson T. A., 2005, ApJ, 618, 569
 Nantais J. et al., 2020, MNRAS, 499, 3061
 Nelson D. et al., 2013, MNRAS, 429, 3353
 Nelson D. et al., 2019, MNRAS, 490, 3234
 Noguchi M., 2018, Nat, 559, 585
 Noguchi M., 2020, MNRAS, 494, L37:wq!
 Noirot G. et al., 2018, ApJ, 859, 38
 Ocvirk P., Pichon C., Teyssier R., 2008, MNRAS, 390, 1326
 Okamoto T., Gao L., Theuns T., 2008, MNRAS, 390, 920
 Old L.J. et al., 2020, MNRAS, 493, 5987
 Oppenheimer B.D. et al., 2010, MNRAS, 406, 2325
 Overzier R.A., 2016, Astron. Astrophys. Rev., 24, 14
 Pacifici C. et al., 2016, ApJ, 824, 45
 Pandya V. et al., 2020, ApJ, 905, 4
 Pearson W.J. et al., 2019, A&A, 631, 51
 Popesso P. et al., 2019, MNRAS, 490, 5285
 Popping G., Behroozi P.S., Peebles M.S., 2015, MNRAS, 449, 477
 Powell M.C. et al., 2017, ApJ, 835, 22
 Prochaska J.X. et al., 2003, ApJ, 595, L9
 Qiu Y. et al., 2021, ApJ, 923, 256
 Queiroz A.B.A. et al., 2020, A&A, 638, A76
 Rees M. J., Ostriker J. P., 1977, MNRAS, 179, 541
 Riebe K. et al., 2013, Astronomisches Nachrichten, 334, 691
 Rodríguez-Puebla A. et al., 2015, ApJ, 799, 130
 Rodríguez-Puebla A. et al., 2020, ApJ, 905, 171
 Saintonge A. et al., 2011, MNRAS, 415, 32
 Santini P. et al., 2017, ApJ, 847, 76
 Schawinski K. et al., 2010, ApJ, 711, 284
 Schawinski K. et al., 2014, MNRAS, 440, 889
 Schaye J. et al., 2003, ApJ, 596, 768
 Schaye J. et al., 2015, MNRAS, 446, 521
 Scholz-Díaz L., Sánchez Almeida J., Dalla Vecchia C., 2021, MNRAS, 505, 4655
 Schreiber C. et al., 2015, A&A, 575, 74
 Schreiber C. et al., 2017, A&A, 599, 134
 Scoville N. et al., 2017, ApJ, 837, 150
 Sijacki D. et al., 2007, MNRAS, 380, 877
 Skelton R.E., et al., 2014, ApJS, 214, 24
 Somerville R.S., Popping G., Trager S.C., 2015, MNRAS, 453, 4337
 Somerville R.S., Primack J.R., 1999, MNRAS, 310, 1087
 Sparre M. et al., 2015, MNRAS, 447, 3548
 Speagle J.S. et al., 2014, ApJS, 214, 15
 Speagle J.S. et al., 2014, ApJS, 214, 15
 Springel V., Di Matteo T., Hernquist L., 2005, ApJ, 620, L79
 Straatman C.M.S. et al., 2016, ApJ, 830, 51
 Sutherland R.S., Dopita M.A., 1993, ApJS, 88, 253
 Tacchella S. et al., 2019, MNRAS, 487, 5416
 Tacconi L.J. et al., 2013, ApJ, 768, 74
 Tacconi L.J. et al., 2018, ApJ, 853, 179
 Teimoorinia H., Bluck A.F.L., Ellison S., 2016, MNRAS, 457, 2086
 Tollet É., Cattaneo A., Macciò A. V., Dutton A. A., Kang X., 2019, MNRAS, 485, 2511
 Tomczak A.R. et al., 2016, ApJ, 817, 118
 Torrey P. et al., 2014, MNRAS, 438, 1985
 Übler H., Naab T., Oser L., Aumer M., Sales L. V., White S. D.M., 2014, MNRAS, 443, 2092
 van de Voort F. et al., 2011, MNRAS, 414, 2458
 van de Voort F., Schaye J., 2012, MNRAS, 423, 2991
 Vincenzo F. et al., 2016, MNRAS, 455, 4183
 Vogelsberger M. et al., 2013, MNRAS, 436, 3031
 Vogelsberger M. et al., 2014, Nature, 509, 177
 Vogelsberger M. et al., 2014, MNRAS, 444, 1518
 Walter F., Brinks E., de Blok W. J. G. et al., 2008, AJ, 136, 2563
 Wang L. et al., 2015, MNRAS, 454, 83
 Wechsler R.H. et al., 2002, ApJ, 568, 52
 Weinberger R. et al., 2018, MNRAS, 479, 4056
 Weinmann S.M. et al., 2012, MNRAS, 426, 2797
 Whitaker K. et al., 2014, ApJ, 795, 104
 Whitaker K. et al., 2021, Nature, 597, 485
 White S.D.M., Frenk C.S., 1991, ApJ, 379, 52
 White C.E., Somerville R.S., Ferguson H.C., ApJ, 799, 201
 Wisnioski E. et al., 2015, ApJ, 799, 209
 Wright R.J. et al., 2020, MNRAS, 498, 1668
 Wu J. et al., 2005, ApJ, 635, L173
 Young J.S., Scoville N.Z., 1991, ARA&A, 29, 581
 Zeimann G.R. et al., 2013, ApJ, 779, 137
 Zhang H.-X. et al., 2012, AJ, 143, 47
 Zhao D.H. et al., 2003, MNRAS, 339, 12
 Zhou S. et al., 2021, ApJ, 916, 38
 Zinger E. et al., 2020, MNRAS, 499, 768

APPENDIX A: NUMERICAL METHODS

A1 Growth of dark matter halos

We follow the parametrization of the mass accretion history of a single halo by [Behroozi, Wechsler & Conroy \(2013\)](#) (APPENDIX H), which gives an excellent fit to Bolshoi ([Klypin, Trujillo-Gomez](#)

& Primack 2011) and Multidark (Riebe et al. 2013) cosmological simulations. This parametrization also solves the problem in Wechsler's parametrization (Wechsler et al. 2002) adopted in previous works (Noguchi 2018, 2020) that mass accretion histories can cross at high redshifts. Although this problem is unlikely to have serious effects for the redshift range we concern, we choose to adopt a more consistent treatment taken in Behroozi, Wechsler & Conroy (2013).

For the concentration parameter of the halo needed in the calculation of the gas cooling time, we follow the result of cosmological simulations for WMAP5 cosmology summarized by Macciò et al. (2008). Namely, the halo concentration at present is given by ,

$$\log C_{\text{vir}} = 0.971 - 0.094 \log(M_{\text{vir}}/[10^{12} h^{-1} M_{\odot}]) \quad (\text{A1})$$

Following Bullock et al. (2001), we assume that the concentration parameter evolves as

$$c(z) = \min \left[K \frac{1+z_c}{1+z}, K \right] \quad (\text{A2})$$

with $K = 3.7$. Here z_c is the collapse redshift of the halo calculated once the present concentration $c(0) = C_{\text{vir}}$ is specified as

$$z_c = c(0)/K \quad (\text{A3})$$

A minimum value on $c(z)$ is imposed following the result by Zhao et al. (2003) to mimic the early growing phase of the halo with nearly constant concentration.

A2 Gas accretion rates

The calculation of gas accretion rate requires the knowledge of dynamical free-fall time and cooling time.

The free-fall time, t_{ff} , is

$$t_{\text{ff}} = \sqrt{\frac{3\pi}{32G\rho_{\text{vir}}}} \quad (\text{A4})$$

where

$$\rho_{\text{vir}} = \frac{3M_{\text{vir}}}{4\pi R_{\text{vir}}^3} \quad (\text{A5})$$

is the average halo density within the virial radius.

In calculating the cooling time, the halo gas is assumed to be in collisional ionization equilibrium with $T = T_{\text{vir}}$. The cooling time, t_{cool} , is then given by

$$t_{\text{cool}} = \frac{3}{2} \mu m_{\text{p}} \frac{kT_{\text{vir}}}{\rho_{\text{hot}} \Lambda(Z_{\text{gas}}, T_{\text{vir}})} \frac{\mu_{\text{e}}^2}{\mu_{\text{e}} - 1} \quad (\text{A6})$$

Here, ρ_{hot} is the density of virialized gas and given by the total mass density at the virial mass multiplied by the cosmic baryon fraction f_{bar} which is assumed to be 0.17. Λ is the normalized cooling function for an ionized gas in collisional ionization equilibrium given by Sutherland & Dopita (1993) that depends on the gas metallicity Z_{gas} and temperature T_{vir} for helium mass abundance of 0.25. No photoionization background is considered here.

We choose a constant gas metallicity, $Z_{\text{gas}} = 0.01$ based on the following consideration. Prochaska et al. (2003) report that their sample of ~ 100 damped Ly α (DLA) systems show the increasing metallicity with the time, from $Z \sim 10^{-2}$ at $z = 4$ to $\sim 10^{-1}$ at $z = 1$. If these DLAs probe innermost regions of halos, the metallicity at the outer halos should be smaller than the reported values. Schaye

et al. (2003) report that the metallicity of the intergalactic medium depends on the overdensity but shows no evidence for evolution. The metallicity increases with the overdensity δ , reaching $\sim 10^{-2}$ at $\delta = 10^2$. Because the virial radius is determined so that the mean overdensity inside the virial radius is ~ 200 , the metallicity at the virial radius at which we calculate the cooling time is likely to be smaller than 10^{-2} . Examination of the effect of varying halo gas metallicity revealed that the results do not change appreciably for $Z < 10^{-2}$. We thus take $Z = 10^{-2}$ as the fiducial value. We do not take into account the metal enrichment from star formation which is unlikely to affect the global gas accretion rate but the innermost region.

The mass accretion rate of the halo gas is calculated as follows. In each time step, the increase of the halo mass during that time step is calculated based on the halo growth model. The gas mass acquired during this period is the halo mass increment multiplied by the cosmic baryon fraction. This gas is assumed to be distributed spherically in accordance with the NFW profile having the concentration parameter as given above. We can calculate the free-fall time and the radiative cooling time for the virial temperature as stated above. Depending on the current location of the halo in the $M_{\text{vir}} - z$ plane (Fig.1) and the adopted scheme, we can determine what timescale, i.e., either the free fall time or the radiative cooling time, we should apply.

This procedure, performed in this form, leads to discontinuous accretion rates when the halo crosses the borders for different accretion domains. The division into different accretion domains shown in Fig.1 is idealized treatment while the transition through a border reported in cosmological simulations is actually more gradual. In order to alleviate this difficulty, we apply smoothing as follows. We consider a rectangular smoothing window which has widths wz in redshift and wm in logarithmic virial mass. Then we evaluate the relative area of each accretion domain included in this window. The newly added gas mass is allotted to each accretion domain according to its fraction and assigned with respective accretion timescale. In the models reported here, window widths of $wz = wm = 0.5$ were taken and each direction was divided into 100 meshes to calculate relative contribution of each domain. This choice was found to retain essential features of the model behaviour while erasing the discontinuity effectively.

A3 Star formation

We follow Blitz & Rosolowsky (2006) in implementing star formation. The gas accreted from the halo is assumed to form a gaseous disc and replenish the interstellar medium (ISM), from which stars are formed.

Star formation rate density, Σ_{SFR} , is given by

$$\frac{\Sigma_{\text{SFR}}}{(\text{M}_{\odot} \text{pc}^{-2} \text{Gyr}^{-1})} = \frac{\epsilon_{\text{SF}}}{(\text{Gyr}^{-1})} \frac{\Sigma_{\text{HCN}}}{(\text{M}_{\odot} \text{pc}^{-2})} \quad (\text{A7})$$

where $\epsilon_{\text{SF}} = 13 \text{Gyr}^{-1}$ (Gao & Solomon 2004; Wu et al. 2005). Here, the surface density of the dense molecular gas is given by,

$$\Sigma_{\text{HCN}} = f_{\text{HCN}} \Sigma_{\text{mol}} \quad (\text{A8})$$

where Σ_{mol} is the surface density of total molecular gas and the ratio

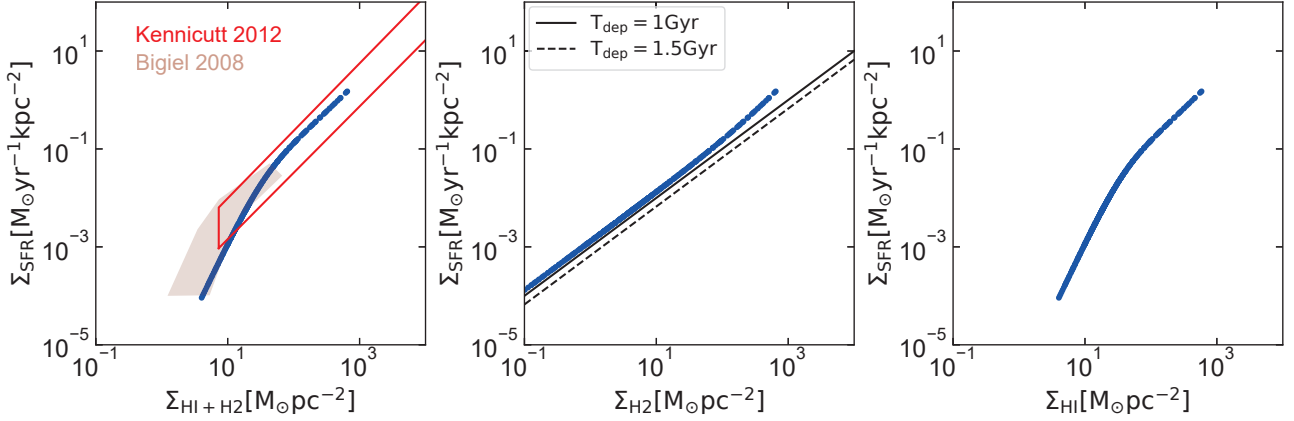


Figure A1. Kennicutt-Schmidt law in the fiducial scheme (blue) compared with the observational data. Left: The star formation rate density as a function of the total gas surface density. The dashed line is an eye-fit to the relation by Kennicutt (2012), whereas the shaded region approximately represents the distribution of galaxies given in Bigiel et al. (2008). Centre: The same as left panel but as a function of the molecular gas surface density. Nearly linear relation for the models is noted. Solid and dashed lines denote the relation for the gas depletion time of 1 Gyr and 1.5 Gyr, respectively. The model depletion time is consistent with the observed value derived by Tacconi et al. (2013). Right: The same as centre panel, but as a function of the neutral gas surface density. Turn-down at low gas density is noted.

f_{HCN} depends on the molecular gas density (Blitz & Rosolowsky 2006) as

$$f_{\text{HCN}} = 0.1 \left[1 + \frac{\Sigma_{\text{mol}}}{(200 M_{\odot} \text{pc}^{-2})} \right] \quad (\text{A9})$$

Total molecular density is derived from the surface density of the cold gas, Σ_{cold} , as

$$\Sigma_{\text{mol}} = f_{\text{mol}} \Sigma_{\text{cold}} \quad (\text{A10})$$

where

$$f_{\text{mol}} = \frac{R_{\text{mol}}}{1 + R_{\text{mol}}} \quad (\text{A11})$$

and

$$R_{\text{mol}} = \left(\frac{P/k}{4.3 \times 10^4} \right)^{0.92} \quad (\text{A12})$$

which we take from Blitz & Rosolowsky (2006) and is valid for $10^{-1} < \Sigma_{\text{mol}}/\Sigma_{\text{HI}} < 10^2$, where the atomic gas surface density is $\Sigma_{\text{HI}} = \Sigma_{\text{cold}} - \Sigma_{\text{mol}}$.

Here, P is the gas pressure at the disc plane and k stands for the Boltzmann constant.

Following the dynamical argument by Elmegreen (1993), the gas pressure in the disc is given by

$$P = \frac{\pi}{2} G \Sigma_{\text{cold}} \left[\Sigma_{\text{cold}} + \left(\frac{\sigma_{\text{cold}}}{\sigma_{\text{star}}} \right) \Sigma_{\text{star}} \right] \quad (\text{A13})$$

where Σ_{star} is the surface density of stars. Surface densities for the cold gas and stars are calculated as $\Sigma_{\text{cold}} \equiv M_{\text{gas}}/(\pi R_{\text{disc}}^2)$ and $\Sigma_{\text{star}} \equiv M_{\text{star}}/(\pi R_{\text{disc}}^2)$, respectively, where the disc radius is set to be λR_{vir} . The spin parameter is taken to be $\lambda = 0.06$. Ratio of the gaseous and stellar velocity dispersions is assumed to be $\sigma_{\text{cold}}/\sigma_{\text{star}} = 0.1$ following Dutton & van den Bosch (2009).

Instant recycling approximation is used to calculate the mass returned to the ISM due to evolution of massive stars with the returned fraction of $R = 0.44$, which is an approximate value for the results reported by Vincenzo et al. (2016) for the Chabrier IMF (Chabrier 2003) for a wide range in metallicity.

The adopted star formation recipe succeeds in reproducing the observed relation between gas surface densities and the star formation rate surface density as shown in Figure A1.

A4 Supernova feedback

Massive stars provide feedback to the surrounding interstellar medium when they explode as supernovae, with the result that some portion of the ISM is ejected from the galaxy. The ejected mass is calculated as

$$\Delta M_{\text{ej}} = \left[\frac{2\epsilon_{\text{FB}} E_{\text{SN}} \eta_{\text{SN}}}{V_e^2} \right] \Delta M_{\text{star}} \quad (\text{A14})$$

where ΔM_{star} is the mass of stars formed in the current time step, ϵ_{FB} is the feedback efficiency, E_{SN} is the energy released by one supernova, and η_{SN} is the number of supernovae produced per one solar mass of stars formed at that step. We take $E_{\text{SN}} = 10^{51}$ erg and $\eta_{\text{SN}} = 8.3 \times 10^{-3}$ following Dutton & van den Bosch (2009). For feedback efficiency we adopt $\epsilon_{\text{FB}} = 0.2$ as the fiducial one.

The escape velocity is calculated as

$$V_e = \sqrt{2GM_{\text{vir}}/R_{\text{vir}}} \quad (\text{A15})$$

We call this model of feedback 'ejective feedback' to distinguish it from 'preventive feedback' described below. We also tried the momentum driven prescription instead of the above energy-driven one as mentioned in the text. In this case, equation (A14) is replaced by

$$\Delta M_{\text{ej}} = \left[\frac{2\epsilon_{\text{FB}} P_{\text{SN}} \eta_{\text{SN}}}{V_e} \right] \Delta M_{\text{star}} \quad (\text{A16})$$

Here, $p_{\text{SN}} = 3 \times 10^4 M_{\odot} \text{kms}^{-1}$ is the momentum produced by one SN taken from [Murray, Quataert & Thompson \(2005\)](#).

A5 Reincorporation (Recycling) of ejected gas

The ultimate fate of the ejected gas is highly uncertain. We assume that some portion of the ejected gas falls back and returns to the galactic disc for further star formation. We use the parametrization by [Mitra, Davé & Finlator \(2015\)](#) for the timescale of reincorporation (recycling) of the ejected gas as

$$t_{\text{rec}} = 0.52 \times 10^9 \text{yr} \times (1+z)^{-0.32} \left(\frac{M_{\text{vir}}}{10^{12} M_{\odot}} \right)^{-0.45} \quad (\text{A17})$$

where the virial mass is given in units of the solar mass.

Although this is obtained as the best fit for their equilibrium model, it was found to reproduce the observation best for the present evolutionary model among many trials with different parameter values.

The mass recycled at each time step is calculated as

$$M_{\text{rec}} = \left(M_{\text{ej}} / t_{\text{rec}} \right) \Delta t \quad (\text{A18})$$

where M_{ej} is the total mass of ejected material present at the current time step (i.e., the reservoir of the ejected material) and Δt is the (constant) length of a single time step. It should be noted that M_{ej} increases by stellar ejective feedback and decreases by recycling. Namely, it is updated at each time step as

$$M_{\text{ej}} = M_{\text{ej}} + \Delta M_{\text{ej}} - M_{\text{rec}} \quad (\text{A19})$$

A6 Preventive feedback

To mimic preventive feedback in a simple form, we reduce the gas accretion rate to the disc calculated as above to the level

$$f_{\text{p}} = f_{\text{pr}} + (1 - f_{\text{pr}}) \left(y + \frac{\pi}{2} \right)$$

where

$$y = \arctan[3(\log M_{\text{vir}} - \log M_{\text{pr}}) / w_{\text{pr}}]$$

Here f_{pr} is the parameter controlling the strength of feedback, M_{pr} is the critical mass below which feedback is significant, and w_{pr} controls how suddenly feedback gets strong with the decreasing halo mass. M_{pr} is a function of redshift and given by

$$\log M_{\text{pr}} = M_0 + z(M_5 - M_0) / 5$$

where M_0 and M_5 are the critical mass at $z = 0$ and 5 , respectively. We take $f_{\text{pr}}=0.3$, $M_0=11.8$, $M_5=11.0$, and $w_{\text{pr}}=0.5$ as the default values unless stated otherwise. For this choice, $f_{\text{p}} \sim 0.65$ at the critical mass. The original accretion rate is multiplied by the calculated factor f_{p} to model preventive feedback.

This paper has been typeset from a $\text{\TeX}/\text{\LaTeX}$ file prepared by the author.